Research Internship (PRE)

Field of Study: SIM/SIM
Scholar Year: 2014-2015

Passive tracer transport in time-dependent corner flows

A mathematical model for the mixing in deep lungs

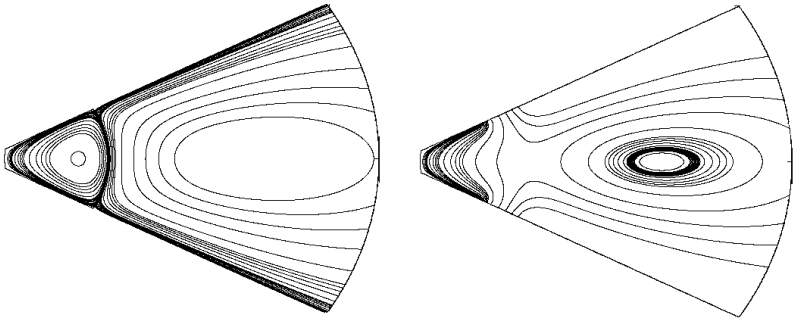

Confidentiality Notice
Non-confidential report and publishable on Internet

Author:
BONNET Benoît

Promotion:
2016

ENSTA ParisTech Tutor:
JEAN Frédéric

Advisor/supervisor:
BRANICKI Michal

Internship from 04/05/2015 to 31/07/2015

Name of the host organism: University of Edinburgh
Address: James Clerk Maxwell Building
King's Buildings
Edinburgh EH9 3JZ
United Kingdom

Confidentiality Notice

This present document is not confidential. It can be communicated outside in paper format or distributed in electronic format.

Abstract

The coming work aims at giving a new mathematical model for the mixing occuring in the deep lungs using dynamical system theory applied to solutions of corner flows problems. This type of model has already been used in a slightly different way by several authors such as Tsuda in [1] or Laine-Pearson and Hydon in [2] in order to describe the same phenomenom.

The approach developed in these articles was based on the KAM theory theory which requires strong hypotheses on the dynamical system in order to be applicable such as having a Hamiltonian structure and being nearly-integrable. Those constraints led the initial models of corner flow generating the dynamical systems to be very simplistic. Thus, the fact that those models can be considered valid in terms of studying mixing properties within an alveola is questionable.

Our study was conveyed with the goal of describing the mixing properties of an alveola without using the very restrictive KAM approach. In order to do so, we first found analytical solutions to corner flows problems in the frame of a refined Stokes flow approximation taking into account the notion of inertia within the fluid. Then we implemented on Matlab mathematical tools in order to describe the properties of interest of the dynamical systems generated by those solutions. Lastly, we applied those tools to a concrete case which bears high resemblance with the one studied in [2]. Since our results were not perfect and not fixable by the time this report was to be submitted, we also present the work which is still in progress.

Acknowledgment

I would like to thank in the first place Michal Branicki, researcher and lecturer at the University of Edinburgh, and my supervisor during this internship for his presence and constant support. He offered me precious guidance throughout my work and it would not have the same shape without him.

I would like to thank my ENSTA supervisor Frédéric Jean for being always receptive and motivative considering this internship and full of guidance considering both my academical and professional projects.

I would like to thank the Erasmus+ organization for the subventions I received that allowed me to travel abroad in the best possible conditions.

I would like to thank my family for their support and for their help in making this internship abroad come true, with a particular thought for my father, Marc Bonnet, for being always present with sound advices that helped me carry out this report.

I would finally like to thank all the people I met at the University of Edinburgh who were all nice and forthcoming and my friends that visited me during my staying to discover this wonderful city

Contents

List of Figures

Introduction

Modeling a pulmonar alveola is something very complex that can be done in various ways. Most of the time, this approach is biologically-oriented, but it can also be physically or mathematically-oriented. One of the less common might be the one we developed here and that aims at mathematically describing the mixing properties of passive tracer within a pulmonar alveola using tools borrowed from the theory of chaotic dynamical systems

A similar study has already been conveyed in a slightly different case by Laine-Pearson and Hydon in [2] . Indeed, they used a model akin to the one we are going to develop and likewise based on results obtained by the renowned fluid dynamics mathematician Keith Moffat in the sixties and eighties in some of his articles such as [3] and [4] dealing with the mathematical properties of Stokes flows within wedge-shaped domains. The biological justification of this model was notably studied in [1].

The basics of the model are the same for Messers Laine-Pearson and Hydon and for us. The very difference in terms of approach that will then lead to substential method divergences is that they rely on the KAM theory to explain the existence of chaos inside the alveola.

The KAM theory, very elegant and useful, is quite restrictive and requires strong hypotheses to be applicable. In order to make this approach feasible, Laine-Pearson and Hydon considered the total flow inside the wedge to be a small perturbation of a leading-order solution for a corner flow driven by a remote potential within the approximation of Stokes flows. The perturbation takes the form of a small time-dependent symmetric boundary motion that yields a new time dependent correcting term.

This way of conveying the study has the concrete advantage of being mathematically elegant, but its very simple character might question its relevance in terms of describing mixing in the deep lungs. Indeed, we thought that this approach could present the following limits :

- in order to apply the KAM theory, the dynamical system needs to be an autonomous Hamiltonian system, nearly integrable and quasi-periodic at most subjected to a small perturbation.
- only the topology of the correcting term is affected by the boundary forcing, making it almost impossible to recover global transport of particles.
- the very simple nature of this approach does not leave much room either for general mathematical considerations about corner flows.

In the following development, we are going to solve the problem of a flow inside a wedge driven by a time-periodic boundary forcing in a completely analytical way. The original features of our work will consist in postulating that the un-perturbed component of the solution is also time dependent and also to determine the exact expression of the related pertubation correcting the Stokes flow approximation inducing a notion of inertia within the flow. This way, we shall obtain general information on the structure of the flow that a formal perturbation and a completely stationary leading order flow could hardly produce.

The aim of our approach will be to determine the exact solutions to two wide classes of corner flows : those that are driven by symmetric and skew-symmetric forcings. In this scope we will then study their mixing properties as well as other interesting features such as global transport or flow reversal. Moreover, we will also describe the effect of the correcting term corresponding to flow inertia on those properties. These solutions will allow us once obtained to solve directly a wide range of much more complicated and general problems such as aperiodic motions, asymmetric ones, etc... Thanks to the linearity of the problem considered here.

In chapter I, we shall detail the method we followed and reproduced in our particular cases to obtain the stream functions associated to given corner flows. In chapter II, we shall describe the different codes we implemented in order to study the properties of the dynamical system by the generated corner flows. Lastly, in chapter III, we shall apply this knowledge to the case of a symmetric-flapping boundary motion and present the numerous development we are still working on in the scope of our article Mr.Branicki and I.

Part I

Mathematical model of a corner flow and resolution for two general classes of forcing problems

The first step of our work, presented in the coming part, is concerned with finding the analytical solution of the problem of a corner flow driven by time dependent boundary forcings in cases as general as possible. In order to do so, we followed a method already developed in [5]. The main motivation was to study particular configurations that would present interesting and distinctive mathematical properties and that would afterward allow to consider more complex and realistic ones.

I.1 Mathematical model for the alveoli

In this section, we recal how the mathematical formulation of the problem can be obtained from the physical model. This approach can be generalised to any kind of situation and will only loose some of its universality upon defining the boundary forcing that we apply.

Let it be noted that even though the method we are going to follow here has already been employed in related cases, the problem we study here is original and was not solved in this fashion before.

I.1.1 Definition and equations of the corner flow

Let us consider a corner flow inside a wedge of total opening angle 2α driven by a perturbation supported remotely from the corner. Let us call $\mathcal{D}$ this domain and $\partial\mathcal{D}$ its boundary such as represented below in a two-dimensional Cartesian frame :

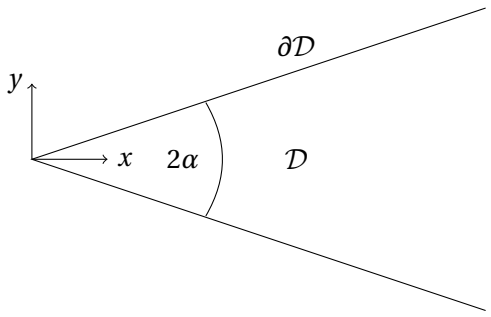

Under the assumption of **incompressible flow**, this type of configuration can be described by the following form of the Navier-Stokes equations :

$$\begin{cases} \dfrac{\partial \mathbf{U}}{\partial t} + (\mathbf{U}.\nabla)\,\mathbf{U} = -\dfrac{1}{\rho}\nabla p + \nu\nabla^2\mathbf{U} \\ \nabla.\mathbf{U} = 0 \end{cases} \quad \text{in } \mathcal{D}\times\mathbb{R}_+ \tag{I.1}$$

where $\mathbf{U}$ and p are the velocity and the pressure field of the fluid, ρ its mass density and ν its kinematic viscosity.

Here, we impose that the velocity on the boundary be equal to a given time-periodic forcing $\mathcal{U}(s,t)$ where s is the arc length coordinate along $\partial\mathcal{D}$. This yields

$$\begin{cases} \mathbf{U}.\mathbf{n} = \mathcal{U}_n(s,t) \\ \mathbf{U}.\mathbf{t} = \mathcal{U}_t(s,t) \end{cases} \quad \text{on } \partial\mathcal{D}\times\mathbb{R}_+ \tag{I.2}$$

Upon taking the curl of (I.1), it is possible to recast the problem in terms of the vorticity $\boldsymbol{\omega} := \nabla\times\mathbf{U}$, assuming the partial derivatives with respect to position and time commute.

Noting furthermore that the vorticity can be expressed as a function of the stream function ψ of the flow through the equation $\boldsymbol{\omega} = -\nabla^2\psi\mathbf{e}_z$, it is possible to write down the flow problem using the unknown ψ as follows

$$\begin{cases} \dfrac{\partial(\nabla^2\psi)}{\partial t} + \dfrac{\partial\left(\nabla^2\psi,\psi\right)}{\partial(x,y)} - \nu\nabla^4\psi = 0 \quad \text{in } \mathcal{D} \\ \dfrac{\partial\psi}{\partial\mathbf{t}} = \mathcal{U}_t(s,t) \ , \ \dfrac{\partial\psi}{\partial\mathbf{n}} = \mathcal{U}_n(s,t) \quad \text{on } \partial\mathcal{D} \end{cases} \tag{I.3}$$

having set

$$\frac{\partial\left(\nabla^2\psi,\psi\right)}{\partial(x,y)} = \frac{\partial(\nabla^2\psi)}{\partial x}\frac{\partial\psi}{\partial y} - \frac{\partial\psi}{\partial x}\frac{\partial(\nabla^2\psi)}{\partial y} \tag{I.4}$$

We can now proceed to non-dimensionalize (I.3) assuming that we are given the following scaling parameters : let $\hat{U}$ and $\hat{\omega}$ be the characteristic amplitude and frequency of the velocity boundary forcing $\mathcal{U}(s,t)$ and $\hat{L}$ be a characteristic length that we will specify later by defining precisely the region of the boundary where $\mathcal{U}$ is non-zero.

We can then non-dimensionalize all the variables involved involved in the problem (I.3) problem through

$$t := \frac{t}{\hat{\omega}} \ , \ x := \hat{L}x \ , \ y := \hat{L}y \ , \ \psi := \hat{L}\hat{U}\psi \tag{I.5}$$

which yields the following non-dimensional formulation of the problem (I.3) :

$$\begin{cases} \eta\dfrac{\partial(\nabla^2\psi)}{\partial t} + \mathrm{Re}\dfrac{\partial\left(\nabla^2\psi,\psi\right)}{\partial(x,y)} - \nabla^4\psi = 0 \quad \text{in } \mathcal{D} \\ \dfrac{\partial\psi}{\partial\mathbf{t}} = \mathcal{U}_t(s,t) \ , \ \dfrac{\partial\psi}{\partial\mathbf{n}} = \mathcal{U}_n(s,t) \quad \text{on } \partial\mathcal{D} \end{cases} \quad , \quad \text{where} \quad \eta = \frac{\hat{\omega}\hat{L}^2}{\nu} \ , \ \mathrm{Re} = \frac{\hat{U}\hat{L}}{\nu} \tag{I.6}$$

I.1.2 Stokes flow approximation and asymptotic expansions

Our flow problem is now formulated in an mathematical and convenient way, but it is still not solvable analytically due to the presence of non linear terms. The next step toward refining this problem is to use asymptotic expansions in the context of the Stokes flow approximation.

In order to solve (I.6), the first reasonable hypothesis that can be made is that the Reynolds number Re of the flow is very small, which will allow to neglect the non linear terms involved in equation (I.6). Moreover, this particular assumption is in agreement with experimental observations that flows in deep lungs can be modelled as Stokes flows.

Additionally, we will also assume that the ratio $\epsilon = \mathrm{Re}/\eta$ is negligible compared to 1. This can indeed be assured by the fact that the orders of magnitude of η and Re can be chosen independently since $\hat{U}$ and $\hat{\omega}$ can change freely.

These two conditions impose the following restrictions on the characteristic parameters : $\hat{U}/\hat{\omega} \ll \hat{L} \ll \nu/\hat{U}$. This hypothesis being made, it is possible to introduce an expansion for small ϵ of the stream function

$$\psi = (\psi_0^{(u)} + \psi_0^{(s)}) + \epsilon(\psi_1^{(u)} + \psi_1^{(s)}) + O(\epsilon^2)$$

Where the (u) exponents denote the unsteady parts of the stream function and (s) the steady parts.

If we introduce this expansion in (I.6) and restrict ourselves to the leading order, we find the following governing equation on $\psi_0^{(u)}$:

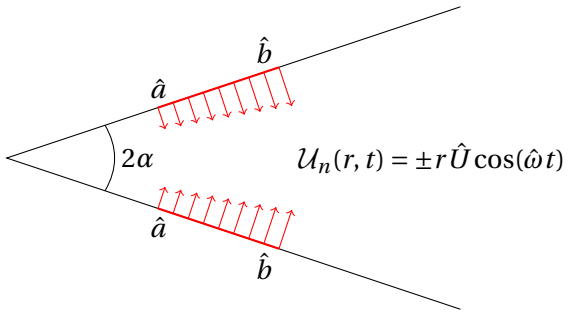

Figure I.1: Illustration of the localized symmetric-flapping boundary condition as defined before

$$\begin{cases} \eta \dfrac{\partial(\nabla^2\psi_0^{(u)})}{\partial t} - \nabla^4\psi_0^{(u)} = 0 \quad \text{in } \mathcal{D} \\ \dfrac{\partial\psi_0^{(u)}}{\partial \mathbf{t}} = \mathcal{U}_t(s,t) \ , \ \dfrac{\partial\psi_0^{(u)}}{\partial \mathbf{n}} = \mathcal{U}_n(s,t) \quad \text{on } \partial\mathcal{D} \end{cases} \tag{I.7}$$

We are now going to expand $\psi_0^{(u)}$ with respect to the parameter η. This will allow us in the next section to obtain an approximate but comparable solution for the stream function. Moreover, the presence of the $O(\eta)$ term will induce a notion of lag within the fluid and thus refine the primary approximation of the flow being "rigid".

Again, we expand $\psi_0^{(u)}$ in the form :

$$\psi_0^{(u)} = \psi_0^{0,(u)} + \eta\psi_0^{1,(u)} + O(\eta^2)$$

Upon identifying contributions with like powers in η, the introduction of this expansion in (I.7) yields the following equations :

$$\begin{cases} \nabla^4\psi_0^{0,(u)} = 0 \quad \text{in } \mathcal{D} \\ \dfrac{\partial\psi_0^{0,(u)}}{\partial \mathbf{t}} = \mathcal{U}_t(s,t) \ , \ \dfrac{\partial\psi_0^{0,(u)}}{\partial \mathbf{n}} = \mathcal{U}_n(s,t) \quad \text{on } \partial\mathcal{D} \end{cases} \ , \ \begin{cases} \nabla^4\psi_0^{1,(u)} - \eta\dfrac{\partial(\nabla^2\psi_0^{0,(u)})}{\partial t} = 0 \quad \text{in } \mathcal{D} \\ \dfrac{\partial\psi_0^{1,(u)}}{\partial \mathbf{t}} = 0 \ , \ \dfrac{\partial\psi_0^{1,(u)}}{\partial \mathbf{n}} = 0 \quad \text{on } \partial\mathcal{D} \end{cases} \tag{I.8}$$

During the following development, we shall calculate the leading order and first order terms of this expansion.

The final step in setting the asymptotic mathematical model of our problem is now to define the boundary forcing $\mathcal{U}(s,t)$.

I.1.3 Definition of the boundary forcing

The choice of the boundary condition we are going to impose is very important. Indeed, as mentioned before, the forcing will induce strong properties on the flow and define distinct classes of solutions with different properties and structures. Moreover, it shall be seen aftwerwards that the parameters most that influences the nature of the flow will be the symmetries in the forcing term.

We chose to detail the whole solving procedure for one of those canonical problems corresponding to a normal localized symmetric forcing.

Let us adopt a polar coordinates setting. Let $\mathcal{U}(r,t)$ be the boundary forcing whose amplitude is proportionate to the normalized distance r from the corner and which will be non-zero only for $r \in [\hat{a},\hat{b}]$, $0 \leqslant \hat{a} < \hat{b}$ as illustrated in figure I.1.

We can now introduce the characteristic length scale $\hat{L} = \hat{a}$ and the variable $b = \hat{b}/\hat{L}$. All taken into account, we can further assume that the different components of the stream function are going to be time-periodic since the forcing is. In this scope, we can write that :

$$\psi_0^{0,(u)}(r,\theta,t) = \mathcal{R}\left[e^{it}\hat{\psi}_0(r,\theta)\right] \quad , \quad \psi_0^{1,(u)}(r,\theta,t) = \mathcal{R}\left[e^{it}\hat{\psi}_1(r,\theta)\right] \tag{I.9}$$

We can finally write the governing equations for the spatial components $\hat{\psi}_0$ and $\hat{\psi}_1$ of the stream function that we are going to solve in the next section :

$$\begin{cases} \nabla^4\hat{\psi}_0 = 0 \quad (r \geqslant 0\ ,\ -\alpha < \theta < \alpha) \\ \dfrac{1}{r}\dfrac{\partial\hat{\psi}_0}{\partial\theta}(r,\pm\alpha) = 0 \\ \dfrac{\partial\hat{\psi}_0}{\partial r}(r,\theta=\pm\alpha) = \begin{cases} 0 \text{ if } r<1 \\ \pm r \text{ if } 1<r<b \\ 0 \text{ if } r>b \end{cases} \end{cases} , \quad \begin{cases} \nabla^4\hat{\psi}_1 - i\eta\nabla^2\hat{\psi}_0 = 0 \quad \text{inside } \mathcal{D} \\ \dfrac{\partial\hat{\psi}_1}{\partial r}(\pm\alpha) = \dfrac{1}{r}(\pm\alpha)\dfrac{\partial\hat{\psi}_1}{\partial\theta} = 0 \end{cases} \tag{I.10}$$

Remark (1). There are reasons why we chose this context to solve our problem.

1. Taking a forcing which is proportional to the distace r to the corner seems more physical and prevents the arising of singularities near said corner.
2. Upon considering the limiting situtation $\hat{a} \to 0$ and $\hat{L} = \hat{b}$ in what precedes, it is possible to recover very easily the particular case corresponding to $\hat{a} = 0$.

Remark (2). As it shall be further detailed later on, defining a boundary forcing that is symmetric or skew-symmetric will be completely equivalent to choosing a class of solutions. Indeed, it will be seen that the topological structure of the solution as well as its global behaviour will mainly depend on the symmetry properties of the forcing.

I.2 Determination of the leading component of the solution $\hat{\psi}_0$

I.2.1 Definition of the Mellin transform and some of its useful properties

The Mellin transform, named after the Finnish mathematician R.H.Mellin (1854 - 1933), is a transformation in the complex field that first arose in a memoir of Riemann dealing with the famous Zeta function. This transform, unlike Laplace and Fourier transforms that were created in order to study phenomena born from physics, is mainly used in mathematical studies and is strongly linked to the Cauchy theory of integration and spectral analysis.

In the context of this work, the Mellin transform will allow us to analytically solve the set of equations (I.10). Hereafter we briefly recall its defition and that of its inverse, which will prove useful during the remainder of our development. For more details, see [6].

Definitin of the Mellin transform For a given function f defined on the positive real axis, the Mellin transform $\mathcal{M}[f]$ of f is a function of the complex variable p defined by :

$$\mathcal{M}[f](p) = \int_0^{+\infty} f(r) r^{p-1} \mathrm{d}r \tag{I.11}$$

Where p belongs to a strip $S(f)$ depending on the function f being transformed, the condition of existence being that $r \longrightarrow r^{\mathcal{R}[p]-1} f(r)$ be integrable.

Remark. The Mellin transform is closely related to Laplace and Fourier transforms and can be, as it is the case for the latter two well known isomorphisms, generalized to distributions. We shall however stick to the simple case of functions in the short development we make here on this mathematical object.

Definition of the inverse Mellin transform Under certain conditions, it is possible to take the inverse Mellin transform of a given function. Let f be a function defined on the positive real axis and c be a real constant such that $\int_0^{+\infty} f(r) r^{c-1} \mathrm{d}r$ exists.

Then, assuming $\mathcal{M}[f]$ is holomorphic in the strip $S(f)$, it is possible define the inverse of the Mellin transform, whereby f is given in terms of its transform by

$$f(r) = \frac{1}{2i\pi} \int_{c-i\infty}^{c+i\infty} \mathcal{M}[f](p) r^{-p} \mathrm{d}p \tag{I.12}$$

Moreover, the function $r \in [0, +\infty[\mapsto f(r)$ is guaranteed to be continuous if $\mathcal{M}[f]$ verifies the condition

$$\left|\mathcal{M}[f](p)\right| \leqslant K|p|^{-2} \tag{I.13}$$

for all p in the strip of holomorphy $S(f)$, where $K > 0$ is constant.

Relationship between the transformation of a function and the transformation of its derivative or its product by a polynomial As indicated before, the following results will hold only within a given strip of holomorphy $S(f)$ depending on the function f being transformed. This assumption being made, it is possible to write the following properties that can easily be verified in the simple case where f is a function.

- ◇ Mellin transform of a derivative of the orignial function :

$$\mathcal{M}\left[\frac{\mathrm{d}^k f}{\mathrm{d}r^k}(r)\right](p) = (-1)^k \left(\prod_{i=1}^{k}(s-i)\right)\mathcal{M}\left[f\right](p-k) \quad \text{where } k \in \mathbb{N}^* \ ; \ (p-k) \in S(f) \tag{I.14}$$

- ◇ Mellin transform of the product of the original function by a power of r

$$\mathcal{M}\left[r^z f(r)\right](p) = \mathcal{M}\left[f\right](p+z) \quad \text{where } z \in \mathbb{C} \ ; \ (p+z) \in S(f) \tag{I.15}$$

Having introduced this very powerful tool and some of its properties, we are now in a position to solve analytically our problem following the method described in the coming sections.

I.2.2 Analytical expression of $\hat{\Psi}_0 = \mathcal{M}[\hat{\psi}_0]$

In order to transform the equation on $\hat{\psi}_0$ given in (I.10) into an equation on $\hat{\Psi}_0 = \mathcal{M}[\hat{\psi}_0]$, we shall multiply said equation by r^{p+3} where p is complex. It shall be verified retrospectively that the following functions vanish quickly enough both when $r \longrightarrow 0$ and $r \longrightarrow +\infty$:

$$r^{p+n}\frac{\partial^n \hat{\psi}_0}{\partial r^n} \ , \ n \in \{0,1,2,3\} \ , \ r^p \frac{\partial^n \hat{\psi}_0}{\partial \theta^n} \ , \ n \in \{1,2\} \ , \ r^{p+1}\frac{\partial \hat{\psi}_0}{\partial r^3 \partial \theta^2} \tag{I.16}$$

These assumptions being made, we can multiply the biharmonic equation on $\hat{\psi}_0$ by r^{p+3} and the corresponding boundary conditions by r^p and integrate them for r running from 0 to $+\infty$.

We thus obtain the following equations on the Mellin transform $\hat{\Psi}_0$ of $\hat{\psi}_0$:

$$\frac{\mathrm{d}^4\hat{\Psi}_0}{\mathrm{d}\theta^4} + \left[p^2 + (p+2)^2\right]\frac{\mathrm{d}^2\hat{\Psi}_0}{\mathrm{d}\theta^2} + p^2(p+2)^2\hat{\Psi}_0 = 0 \tag{I.17a}$$

$$\hat{\Psi}_0(p, \pm\alpha) = \mp\frac{b^{p+2}-1}{p(p+2)} \ , \ \frac{\mathrm{d}\hat{\Psi}_0}{\mathrm{d}\theta}(p, \pm\alpha) = 0 \tag{I.17b}$$

Before solving the ODE above, let us remark that given the configuration of the flow we study, the velocity field is going to be symmetric with respect to the axis $\theta = 0$. Therefore, the corresponding stream function is going to be skew-symmetric with respect to the same axis. Knowing this and solving the characeristic polynomial of the equation yields the following form for its solution : $\hat{\Psi}_0 = A\sin(p\theta) + B\sin[(p+2)\theta]$

The unique solution corresponding to the boundary conditions imposed here is the following function

$$\hat{\Psi}_0(p,\theta) = \frac{(b^{p+2}-1)}{W(p)}\left[\frac{\cos[(p+2)\alpha]\sin(p\theta)}{p} - \frac{\cos(p\alpha)\sin[(p+2)\theta]}{p+2}\right] \tag{I.18}$$

where $W(p) = (p+1)\sin(2\alpha) - \sin[2(p+1)\alpha]$

Remark. As it will be seen later on, the W function is probably the most crucial component of the solution. It will dictate its main structure and its asymptotic behaviour for small r. More importantly, it depends only on the symmetry of the problem. In the case of a symmetric tangential forcing, the analogue function W would the same, and in the case of an skew-symmetric forcing (be it tangential or normal), this function is roughly similar and given by : $W_{\text{asy}}(p) = (p+1)\sin(2\alpha) + \sin[2(p+1)\alpha]$.

Keeping this in mind will be of great help while going through the appendices.

I.2.3 Inverting the Mellin transform

Now that we managed to find the expression of the Mellin transform of $\hat{\psi}_0$ as a function of p there only remains to take its inverse to have the analytical expression of $\hat{\psi}_0$. As it can be seen in the definition of the inverse transform, this will require us to integrate $\hat{\Psi}_0$ on a properly chosen vertical axis $\mathcal{R}[p] = c$ of the complex field. In the case we study, it can be shown restrospectively using the condition used to define (I.12) that $c = -1$ is an adequate choice.

The order 0 part of the stream function can then be written as

$$\hat{\psi}_0(r,\theta) = \frac{1}{2i\pi}\int_{-1-i\infty}^{-1+i\infty}\left(\frac{b^2(\frac{b}{r})^p - \frac{1}{r^p}}{W(p)}\right)\left[\frac{\cos[(p+2)\alpha]\sin(p\theta)}{p} - \frac{\cos(p\alpha)\sin[(p+2)\theta]}{p+2}\right]\mathrm{d}p \tag{I.19}$$

In order to calculate this integral, we are going to close this axis into a contour at a far distance of the origin which choice will depend on r and use the well known residue theorem. In order to do so we shall now explain how to choose this contour and study the poles of $r^{-p}\hat{\Psi}_0(p,\theta)$.

Choice of the contour of integration As it will be seen in the next section, $r^{-p}\hat{\Psi}_0(p,\theta)$ has an infinity of poles in the complex field which real parts diverge to infinity in both half-complex planes $\mathcal{R}[p] > -1$ and $\mathcal{R}[p] < -1$. Thus, the choice of the contour will depend on the ratios (b/r) and $1/r$ as follows :

(i) If $r < 1$, the contour will be closed in the half plane $\mathcal{R}[p] < -1$ for the integral to converge and all the pole will have a winding number equal to 1.

(ii) If $r > b$, we shall close the contour in the half plane $\mathcal{R}[p] > -1$, this leading to poles having a winding number equal to (-1).

(iii) If $1 < r < b$, we need to split the two parts $(b/r)^p$ and $(1/r)^p$ of the integral and close the contour in $\mathcal{R}[p] < -1$ for the first one and in $\mathcal{R}[p] > -1$ for the second one.

Quick analysis of the poles of $\hat{\Psi}_0$ and analytical expression of $\hat{\psi}_0$ In order to analyse the poles of $r^{-p}\hat{\Psi}_0(p,\theta)$, we need to examine carefully the function W defined previously. The complete study of this function was made by Moffatt in [4].

The function W vanishes evidently at $\{-2,-1,0\}$. Moreover, if the angle 2α of the wedge is strictly inferior to a critical value $2\alpha_c \simeq 159°$ given as well by Moffatt in [4], these are the only purely real zeros of W. In the scope of our work, we stuck to this hypothesis since we were interested in the study of the wedge configuration for accute angles 2α .

The other zeros of W are forming a sequence of complex numbers that we shall evaluate numerically . Those complex numbers, denoted $(p_n)_{n\in\mathbb{Z}}$ in what follows, verify the following properties :

$$\forall n > 1\ ,\ \mathcal{R}[p_n] > 0 \tag{I.20a}$$

$$\text{if}\quad W(p_n) = 0\quad \text{then}\quad \begin{cases} W(-p_n-2) = 0 \\ W(\overline{p_n}) = 0 \end{cases} \tag{I.20b}$$

It can also easily be demonstrated that there exists only one doublet of complex conjugate zeros $(p_{2n}, p_{2n+1})_{n\geq 1}$ of W within each strip of the form $S_{2n} = \left[\frac{n\pi}{\alpha} - 1, \frac{\pi}{\alpha}\left(n+\frac{1}{2}\right) - 1\right]$ of the half plane $\mathcal{R}[p] > 0$. This means in particular considering (I.20b) that $\mathcal{R}[p_n] \underset{n\to\pm\infty}{\longrightarrow} \pm\infty$ and justifies our contours choice made before.

From now on, we will note this sequence $(p_n)_{n\in\mathbb{Z}}$ where $\{p_{-1}, p_0, p_1\} = \{-2,-1,0\}$ and where $(p_n)_{|n|>1}$ is the sequence of complex numbers described hereabove.

Using some basic algebra, it can be shown that the poles of $\hat{\Psi}_0$ are exactly the $(p_n)_{|n|>1}$, $p = 0$ and $p = -2$ when $1 < r < b$ and the integrals are split.

We finally obtain the following piecewise expression for $\hat{\psi}_0$:

$$\hat{\psi}_0(r,\theta) = \begin{cases} \displaystyle\sum_{m<-1} \left(\frac{b^{p_m+2}-1}{r^{p_m}}\right)\left(\frac{f_m^1(\theta,\alpha)}{p_m} - \frac{f_m^2(\theta,\alpha)}{p_m+2}\right) & \text{if } r \leqslant 1 \\ (1-r^2)g(\theta,\alpha) + \displaystyle\sum_{m<-1} \frac{b^{p_m+2}}{r^{p_m}}\left(\frac{f_m^1(\theta,\alpha)}{p_m} - \frac{f_m^2(\theta,\alpha)}{p_m+2}\right) + \sum_{m>1} \frac{1}{r^{p_m}}\left(\frac{f_m^1(\theta,\alpha)}{p_m} - \frac{f_m^2(\theta,\alpha)}{p_m+2}\right) & \text{if } 1 \leqslant r \leqslant b \\ (1-b^2)g(\theta,\alpha) - \displaystyle\sum_{m>1} \left(\frac{b^{p_m+2}-1}{r^{p_m}}\right)\left(\frac{f_m^1(\theta,\alpha)}{p_m} - \frac{f_m^2(\theta,\alpha)}{p_m+2}\right) & \text{if } r \geqslant b \end{cases} \tag{I.21}$$

where

$$f_m^1(\theta,\alpha) = \frac{\cos[(p_m+2)\alpha]\sin(p_m\theta)}{\sin(2\alpha) - 2\alpha\cos[2(p_m+1)\alpha]} \quad , \quad f_m^2(\theta,\alpha) = \frac{\cos(p_m\alpha)\sin[(p_m+2)\theta]}{\sin(2\alpha) - 2\alpha\cos[2(p_m+1)\alpha]}$$
$$\text{and} \quad g(\theta,\alpha) = \frac{\theta\cos(2\alpha) - \frac{1}{2}\sin(2\theta)}{\sin(2\alpha) - 2\alpha\cos(2\alpha)} \tag{I.22}$$

Note that all the expressions in (I.21) and (I.22) are completely legit since the denominators of f_m^1, f_m^2 and g are non zero for any wedge geometry where the total angle 2α is accute and for all m.

Moreover, it can now be checked retrospectively that all the asumptions made on the stream function in terms of integrability and fast decay for both small and large r (see (I.16)) are verified.

It can also be easily verified numerically using (I.14) and (I.15) that the function $p \mapsto \left|p^2\mathcal{M}\left[\nabla^4\hat{\psi}_0\right](p)\right|$ is bounded within the maximal holomorphy strip $S(\hat{\psi}_0)$ given by

$$S(\hat{\psi}_0) = \left\{\ p \in \mathbb{C} \ \middle|\ \mathcal{R}[-p_2-2] < \mathcal{R}[p] < \mathcal{R}[p_2]\ \right\} \tag{I.23}$$

We can thus assert that the function $\hat{\psi}_0$ given by (I.21) and (I.22) is $\mathcal{C}^4$ with respect to r and θ as expected. This particular result will prove very useful in the appendix section dealing with the convergence of the different series expansions arising in the expressions of the stream functions and velocity fields.

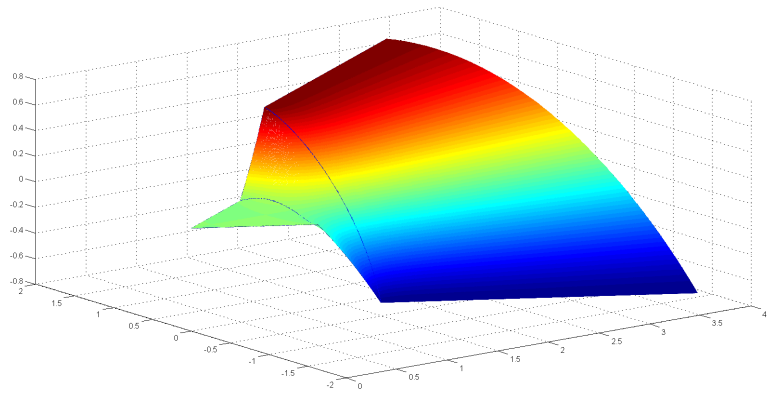

Figure I.2: Plot of the order 0 stream function $\hat{\psi}_0$ in cartesian coordinates. The two shaded lines on the plot were added manually and correspond to the interfaces $r = 1$ and $r = b$ so that they can easily be seen

I.3 Determination of the first order correction $\hat{\psi}_1$

We established in section I.2 the solution for the order 0 stream function, using the same method by Moffatt in [3] and [4]. We are now going to determine the first order correction of this stream function in the approximation of Stokes flow using the Laplacian of $\hat{\psi}_0$ which will bring a non-zero term on the right side of the biharmonic equation (I.10).

Analytical expression of $\hat{\Psi}_1 = \mathcal{M}[\hat{\psi}_1]$ As in section I.2, we multiply by r^{p+3} and r^p the field equation and the boundary conditions on $\hat{\psi}_1$ in (I.10) and integrate from $r = 0$ to $r = +\infty$ while being careful redarding the expression of $\nabla^2\hat{\psi}_0$ on the different integration intervales. Besides, the fact that the right member of the equation must be integrable yields the following constraint on p

$$-\mathcal{R}[p_2] - 2 < \mathcal{R}[p] < -2 \tag{I.24}$$

After some algebra and regouping, we can obtain the following equation for $\hat{\Psi}_1 = \mathcal{M}[\hat{\psi}_1]$ in the Mellin domain.

$$\begin{cases} \dfrac{\mathrm{d}^4\hat{\Psi}_1}{\mathrm{d}\theta^4} + \left[p^2 + (p+2)^2\right]\dfrac{\mathrm{d}^2\hat{\Psi}_1}{\mathrm{d}\theta^2} + p^2(p+2)^2\hat{\Psi}_1 = \dfrac{2i(b^{p+4}-1)}{(p+2)[\sin(2\alpha) - 2\alpha\cos(2\alpha)]}\sin(2\theta) \\ \qquad\qquad - \dfrac{4i(b^{p+4}-1)\cos(2\alpha)}{(p+4)[\sin(2\alpha) - 2\alpha\cos(2\alpha)]}\theta \\ \qquad\qquad + 4i(b^{p+4}-1)\displaystyle\sum_{m>1}\left[\frac{(p_m+1)f_m^2(\theta,\alpha)}{(p_m+2)(p-p_m-2)} - \frac{(p_m+1)f_m^1(\theta,\alpha)}{p_m(p+p_m+4)}\right] \\ \hat{\Psi}_1(\pm\alpha) = \dfrac{\mathrm{d}\hat{\Psi}_1}{\mathrm{d}\theta}(\pm\alpha) = 0 \end{cases} \tag{I.25}$$

Since all the forcing terms are odd functions of θ, we can now proceed to search the solution to this equation in the form :

$$\hat{\Psi}_1(p,\theta) = \underbrace{A\sin(\theta) + B\sin[(p+2)\theta]}_{\text{solves homogene ODE}} + \underbrace{C\sin(2\theta) + D\theta + \sum_{m>1}\left[\beta_m\sin(p_m\theta) + \gamma_m\sin[(p_m+2)\theta]\right]}_{\text{particular solution}}$$

The function $\hat{\Psi}_1$ satisfying the boundary conditions given in (I.25) takes the rather complicate form :

$$\begin{aligned} \hat{\Psi}_1(p,\theta) =& Z\left(4f_1^Z(p,\theta) + 2f_2^Z(p,\theta)\right) + \sum_{m>1}\left[X_m f_m^X(p,\theta) + Y_m f_m^Y(p,\theta)\right] \\ =& \frac{4i(b^{p+4}-1)\cos(2\alpha)Z}{p^2(p+2)^2(p+4)W(p)}\left[-W(p)\theta - \Omega(p+2)\sin(p\theta) + \Omega(p)\sin[(p+2)\theta]\right] \\ &+ \frac{2i(b^{p+4}-1)Z}{p(p-2)(p+2)^2(p+4)W(p)}\left[W(p)\sin(2\theta) + \mathcal{U}_2(p)\sin(p\theta) + \mathcal{V}_2(p)\sin[(p+2)\theta]\right] \\ &- 4i(b^{p+4}-1)\sum_{m>1}X_m\frac{\mathcal{U}_{p_m}(p)\sin(p\theta) + \mathcal{V}_{p_m}(p)\sin[(p+2)\theta] + W(p)\sin(p_m\theta)}{W(p)(p+p_m+4)(p-p_m)(p+p_m)(p+p_m+2)(p-p_m+2)} \\ &+ 4i(b^{p+4}-1)\sum_{m>1}Y_m\frac{\mathcal{U}_{p_m+2}(p)\sin(p\theta) + \mathcal{V}_{p_m+2}(p)\sin[(p+2)\theta] + W(p)\sin[(p_m+2)\theta]}{W(p)(p+p_m+4)(p-p_m)(p-p_m-2)(p+p_m+2)(p-p_m+2)} \end{aligned} \tag{I.26}$$

where

$$\begin{cases} \mathcal{U}_\xi(p) = (p+2)\cos[(p+2)\alpha]\sin(\xi\alpha) - \xi\cos(\xi\alpha)\sin[(p+2)\alpha] \\ \mathcal{V}_\xi(p) = \xi\cos(\xi\alpha)\sin(p\alpha) - p\cos(p\alpha)\sin(\xi\alpha) \end{cases}, \quad \begin{cases} W(p) = (p+1)\sin(2\alpha) - \sin[2(p+1)\alpha] \\ \Omega(p) = p\cos(p\alpha) - \sin(p\alpha) \end{cases} \tag{I.27}$$

and

$$\forall m > 1 \quad \begin{cases} X_m = \dfrac{(p_m+1)\cos[(p_m+2)\alpha]}{p_m\left(\sin(2\alpha) - 2\alpha\cos[2(p_m+1)\alpha]\right)} \\ Y_m = \dfrac{(p_m+1)\cos(p_m\alpha)}{(p_m+2)\left(\sin(2\alpha) - 2\alpha\cos[2(p_m+1)\alpha]\right)} \\ Z = \dfrac{1}{\sin(2\alpha) - 2\alpha\cos(2\alpha)} \end{cases} \tag{I.28}$$

Inverting the Mellin transform It is now possible, by carefully applying the same method we did for $\hat{\psi}_0$, to determine the Mellin inverse of $\hat{\Psi}_1$.

As we did before, we will have to complete the vertical axis of integration $\mathcal{R}[p] = c$ into different contours depending on whether $r < 1$, $1 < r < b$ or $r > b$ in order to apply the residue theorem. For each value of m, the functions f_m^X and f_m^Y have the following poles, all of which are simple :

$$\begin{aligned} &\diamond \ \textbf{(i1)} \ \ p = -p_m - 4 \ \ \textbf{(ii)} \ \ p = p_k \ \ \textbf{(iii)} \ \ p = -p_k - 2 \ , \ k = 1,2,... \ \text{for} \ \ f_m^X \\ &\diamond \ \textbf{(i2)} \ \ p = p_m - 2 \ \ \textbf{(ii)} \ \ p = p_k \ \ \textbf{(iii)} \ \ p = -p_k - 2 \ , \ k = 1,2,... \ \text{for} \ \ f_m^Y \end{aligned} \tag{I.29}$$

and the functions f_1^Z and f_2^Z respectively have simple poles at **(iv)** $p = -4$ (only when $1 < r < b$) and **(v)** $p = -2$ in addition to **(ii)** and **(iii)**. It can be shown using a significant amount of algebra that all the other singularities are removable. Not forgetting the constraint (I.24) induces on the choice of c, it will be possible to show aftwerard that $c = -3$ is adequate.

The expression of the function $\hat{\psi}_1$ takes then a rather voluminous piecewise form, which is shown in full detail in the appendices (A.1), (A.2) and (A.3).

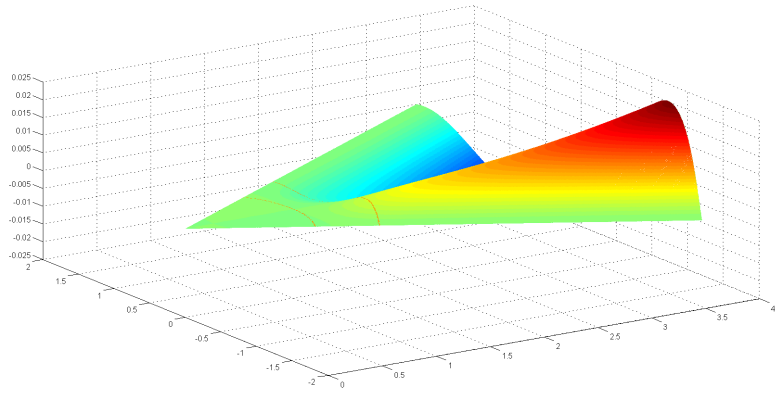

Figure I.3: Plot of the order 1 stream function $\hat{\psi}_1$ in cartesian coordinates. Again, the shaded lines were added so the different areas can be easily identified

The careful reader will remark that the expression of the stream function far from the corner given by the appendix equation (A.2) includes a divergent term proportional to r^2. This term leads to divergent radial and angular velocities, which at first might seem absurd. However, it can be easily shown that the total flux of fluid going through any arc in the outer area is equal to zero, giving some consistency to the solution.

The solution we found is thus plausible, but not valid for any given r. It is possible to numerically determine the critical value of r from which the expansion does not hold anymore. This value is defined as the limit radius such that a condition of the form $\eta\hat{\psi}_1 \leqslant \gamma\hat{\psi}_0$ where γ can be chosen arbitrary such that $\hat{\psi}_1 \lesssim \gamma\hat{\psi}_0$ gives a suitable relative order of magnitude between $\hat{\psi}_1$ and $\hat{\psi}_0$ remains valid.

For instance, for $\gamma = 1/10$ and $\alpha = \pi/6$, a comparison of the different leading terms roughly yields the condition $r \leqslant \frac{4.45}{\sqrt{\eta}}$, which is not very restricitive considering the typical ranges within which we study the mixing properties, namely $r \in \left[0, \frac{3}{2}b\right]$ where typically $1.5 \leqslant b \leqslant 2.5$.

I.4 Structure and properties of the two classes of solutions

We are now going to focus on some interesting features of the solutions to the symmetric and skew-symmetric boundary forcing problems, but first, let us do a slight yet important precision here.

We talked several times about classes of solutions. Indeed, the symmetry imposed on the boundary forcing will entirely define the W function which zeros are the main parameter defining the structure of solutions.

In the exact same way that we proceeded for a symmetric,normal and radially linear boundary condition (see section I.1), we solved the problem in the case of an skew-symmetric normal forcing, even though it is not detailed here. The analytical solutions to this problem are displayed in the appendix B.

Another skew-symmetric case corresponding to an oscillatory tangential motion was also solved by Mr.Branicki some times ago in an un-published draft. Let it be noted that in the tangential case, the forcing is not radially linear and always localized within a segment $[a,b]$ with $a>0$ to prevent any singularity from arising. The solutions are given in the appendix C. Even though we did not do it because it was not a top-priority consideration in the scope of this study, it would also be possible to solve the problem in the case of an symmetric tangential motion.

As mentioned before, these solutions (however slightly different) do share similarities and common properties, some of which we are going elaborate on right now.

I.4.1 Asymptotic structure of the flow near the corner

As mentionned previously, the main parameter influencing the structure of the flow inside the wedge is the symmetry of the boundary forcing. This (skew-)symmetry is reverberated within the whole flow and gives to it a distinctive structure.

However, we saw that other parameters could play a different yet important role on the nature of the flow, such as the type of forcing (tangential or normal), its amplitude (equal to $\hat{U}$ or to $r\hat{U}$), the support of the forcing is non-zero, etc... But none of these other parameters should have any influence on the asymptotic behaviour of the flow near the corner. Indeed, from this point of view, any kind of forcing would only be seen as a remote perturbation and the flow structure should then not be affected by it.

This is something that we will analytically verify in (I.4.1). We will also show in (I.4.1) that not only do the $O(1)$ and $O(\eta)$ component induce the same structure on the flow near the corner, but also that it effectively does not depend on the type of forcing used as long as the symmetry is the same.

Structure induced by the solution of the Stokes flow approximation in the case of an skew-symmetric forcing

Let us now observe the asymptotic structure for small r of a corner flow driven by an skew-symmetric normal boundary forcing proportionate to the radius r. To do so, we will be following the same path Keith Moffatt took in the case of an skew-symmetric oscillating sleeves-like boundary forcing in his article [3].

For r sufficiently small, the dominant terms in the expression of $\hat{\psi}_0$ are the two first of the series expansion given by (B.3), meaning

$$\hat{\psi}_0(r,\theta) \underset{r\to 0}{\sim} -2\,\mathcal{R}\left[r^{p_2+2}(b^{-p_2}-1)\left(\frac{f_2^1(\theta,\alpha)}{p_2}-\frac{f_2^2(\theta,\alpha)}{p_2+2}\right)\right] \tag{I.30}$$

where

$$f_2^1(\alpha)=\frac{\sin[(p_2+2)\alpha]\cos(p_2\theta)}{\sin(2\alpha)-2\alpha\cos[2(p_2+1)\alpha]} \quad \text{and} \quad f_2^2(\alpha)=\frac{\sin(p_2\alpha)\cos[(p_2+2)\theta]}{\sin(2\alpha)-2\alpha\cos[2(p_2+1)\alpha]} \tag{I.31}$$

which yields for v_θ

$$v_\theta(r,\theta)=-\frac{\partial\hat{\psi}_0}{\partial r}(r,\theta) \underset{r\to 0}{\sim} 2\,\mathcal{R}\left[r^{p_2+1}(p_2+2)(b^{-p_2}-1)\left(\frac{f_2^1(\theta,\alpha)}{p_2}-\frac{f_2^2(\theta,\alpha)}{p_2+2}\right)\right] \tag{I.32}$$

Let us now assume that θ is small aswell. This assumption leads to

$$\begin{aligned} &v_\theta(r,\theta) \underset{r,\theta\to 0}{\sim} 2\,\mathcal{R}\left[r^{p_2+1}(p_2+2)(b^{-p_2}-1)\left[h_2^1(\alpha)-h_2^2(\alpha)\right]\right] \\ &\text{with} \quad h_2^1(\alpha)=\frac{\sin[(p_2+2)\alpha]}{\sin(2\alpha)-2\alpha\cos[2(p_2+1)\alpha]} \quad \text{and} \quad h_2^2(\alpha)=\frac{\sin(p_2\alpha)}{\sin(2\alpha)-2\alpha\cos[2(p_2+1)\alpha]} \end{aligned} \tag{I.33}$$

Introduce the two constants C_M and C_A defined by

$$\begin{cases} C_M=\left|p_2+2\right|\left|b^{-p_2}-1\right|\left|h_2^1(\alpha)-h_2^2(\alpha)\right| \\ C_A=\arg\left(p_2+2\right)+\arg\left(b^{-p_2}-1\right)+\arg\left(h_2^1(\alpha)-h_2^2(\alpha)\right) \end{cases} \tag{I.34}$$

where $\xi_2=\mathbb{R}[p_2]$ and $\eta_2=\mathbb{I}[p_2]$ (I.33) then yields

$$v_\theta(r,\theta) \underset{r,\theta\to 0}{\sim} 2r^{\xi_2+1}C_M\cos\left[\eta_2\ln(r)+C_A\right] \tag{I.35}$$

Since r is small, $\ln(r)$ is going to be negative and it can be shown easily that v_θ will oscillate, its sign changing at each r_k such that

$$\eta_2 \ln(r_k) + C_A = \pi\left(k - \frac{1}{2}\right) \iff r_k = \exp\left(\frac{1}{\eta_2}\left[\pi\left(k-\frac{1}{2}\right) - C_A\right]\right) \quad \text{where } k \in \mathbb{Z}^- \tag{I.36}$$

and reaching its extrema in $r_{k-1/2}$. One can then recognize that this behaviour describes a progression of small eddies centered along the line $\theta = 0$ in $r_{k-1/2}$.

Furthermore, it can be observed that the progression is geometric both for the centers' sequence $(r_{k-1/2})$ and the maximal amplitudes' sequence $|v_\theta(r_{k-1/2},\theta)|$. Indeed

$$\forall k \in \mathbb{Z}^- \ , \ \forall \theta \ \ , \ \ \frac{r_{k+1/2}}{r_{k-1/2}} = \exp\left(\frac{\pi}{\eta_2}\right) \ \text{ and } \ \frac{|v_\theta(r_{k+1/2},\theta)|}{|v_\theta(r_{k-1/2},\theta)|} = \exp\left(\frac{\xi_2 \pi}{\eta_2}\right) \tag{I.37}$$

As announced, the structure we obtain here, which is the one of a geometrically progressing eddies sequence, is exactly the same as that described by Moffat in [3] in the case of an skew-symmetric oscillating sleeves motion.

Structure induced by the order 1 correction

Similarly, it can be shown that the strucutre induced by the $O(\eta)$ correction is the same as the one induced by the $O(1)$ term.

For $r \to 0$, the leading terms in $\hat{\psi}_1$ are given by

$$\begin{aligned}
\mathcal{I}\left[\hat{\psi}_1(r,\theta)\right] =& 2\frac{(b^{-p_2+2}-1)\left[p_m \sin(p_{-2}\alpha)\cos[(p_{-2}+2)\theta] - (p_{-2}+2)\sin[(p_{-2}+2)\alpha]\cos(p_{-2}\theta)\right]}{W'(p_{-2})p_{-2}^2(p_{-2}+2)^2(p_{-2}+4)} r^{p_2+2} \\
&+ -4X_2(b^{p_2}-1)\frac{\mathcal{U}'_{p_2}(-p_2-2)\cos[(p_2+2)\theta] + \left[\mathcal{V}'_{p_2}(-p_2-2) - W'(-p_2-2)\right]\cos(p_2\theta)]}{16W'(-p_2-2)(p_2+1)p_2 W'(-p_2-2)} r^{p_2+2} \\
&+ r^{p_2+2}\sum_{n>2} X_n(b^{-p_2+2}-1)\frac{\mathcal{U}_{p_{-2}}(p_{-2})\cos(p_{-2}\theta) + \mathcal{V}_{p_{-2}}(p_{-2})\cos[(p_{-2}+2)\theta]}{W'(p_{-2})(p_n+p_{-2}+4)(p_n+p_{-2}+2)(p_n-p_{-2}+2)(p_n-p_{-2})(p_n+p_{-2})} \\
&+4Y_2(b^{-p_2+2}-1)\frac{\mathcal{V}'_{p_2+2}(-p_2-2)\cos(p_2\theta) + \left[\mathcal{U}'_{p_2+2}(-p_2-2) - W'(-p_2-2)\right]\cos[(p_2+2)\theta]}{16W'(-p_2-2)(p_2+2)(p_2+1)p_2 r^{-p_2-2}} \\
&- r^{p_2+2}\sum_{n>2} Y_n(b^{p_{-2}+4}-1)\frac{\mathcal{U}_{p_{-2}+2}(p_{-2})\cos(p_{-2}\theta) + \mathcal{V}_{p_{-2}+2}(p_{-2})\cos[(p_{-2}+2)\theta]}{W'(p_{-2})(p_n+p_{-2}+4)(p_n+p_{-2}+2)(p_n-p_{-2}+2)(p_n-p_{-2})(p_n+p_{-2})}
\end{aligned} \tag{I.38}$$

From this expression, it is possible to determine the angular velocity $\tilde{v}_\theta$ generated by $\hat{\psi}_1$ near the corner.

Upon linearizing (I.38) for $\theta \to 0$ and defining two constants $\tilde{C}_M$ and $\tilde{C}_A$ in the same way as in (I.34), it is possible to show that

$$\tilde{v}_\theta(r,\theta) \underset{r,\theta\to 0}{\sim} 2r^{\xi_2+1}\tilde{C}_M \cos\left[\eta_2 \ln(r) + \tilde{C}_A\right] \tag{I.39}$$

Thus, the angular velocity for small r close to the axis $\theta = 0$ has the same structure as the one generated by the leading order term and their behaviours are identical.

This is consistent with the fact that $\hat{\psi}_1$ is the solution of a problem with a forcing $\eta\nabla^2\hat{\psi}_0$ and zero-velocity boundary conditions. Indeed, the symmetric properties of $\hat{\psi}_0$ are preserved by the operator ∇^2 and the Mellin transform and thus transmitted to $\hat{\psi}_1$. Moreover, the forcing term is almost non existent near the corner as the flow grows more and more viscous. Asymptotically, this forcing can also be seen as a remote perturbation driving a flow which was bestowed upon the property of being skew-symmetric.

In the symmetric case

It is possible to perform the same kind of analysis in the symmetric case. The corresponding behaviour is that of geometric sequences of eddies on each side of the separatrix $\theta = 0$ after linearizing the leading order terms given by (A.1).

We will now deal with another interesting behaviour arising within the fluid that involves these sequences of eddies and that might present an interest in terms of mixing properties qualitatively speaking.

I.4.2 Flow reversal

As it can be seen in section (I.1), the solution $\psi(r,\theta,t)$ to a problem formulated as (I.10) can be written $\psi(r,\theta,t) = \hat{\psi}_0(r,\theta)\cos(t)$ at the leading order and $\psi(r,\theta,t) = \hat{\psi}_0(r,\theta)\cos(t) - \eta\hat{\psi}_1(r,\theta)\sin(t)$ when the $O(\eta)$ correction is added.

As mentioned before, adding this correcting term brings a notion of inertia into the fluid, meaning that any information that was previously propagated instantaneously now takes a finite time to do so. This very consideration is visible in a very interesting way in a phenomenom called the flow reversal that Messers Branicki and Moffatt studied in [5].

The phenomenom of flow reversal occurs when time reaches $t = \pi/2$ and $\hat{\psi}_0$ changes sign throughout the whole fluid. This corresponds to the moment when the flapping changes direction, switching from an inward to an outward motion or the other way around. If the only component taken into consideration is the $O(1)$, this switching is instantatneous. However, when the $O(\eta)$ term is added, an intriguing feature can be observed. Indeed, the reversal will not occur instantaneously at $t = \pi/2$ but for $t \in [\pi/2 - \delta, \pi/2 + \delta]$ and can thus be monitored.

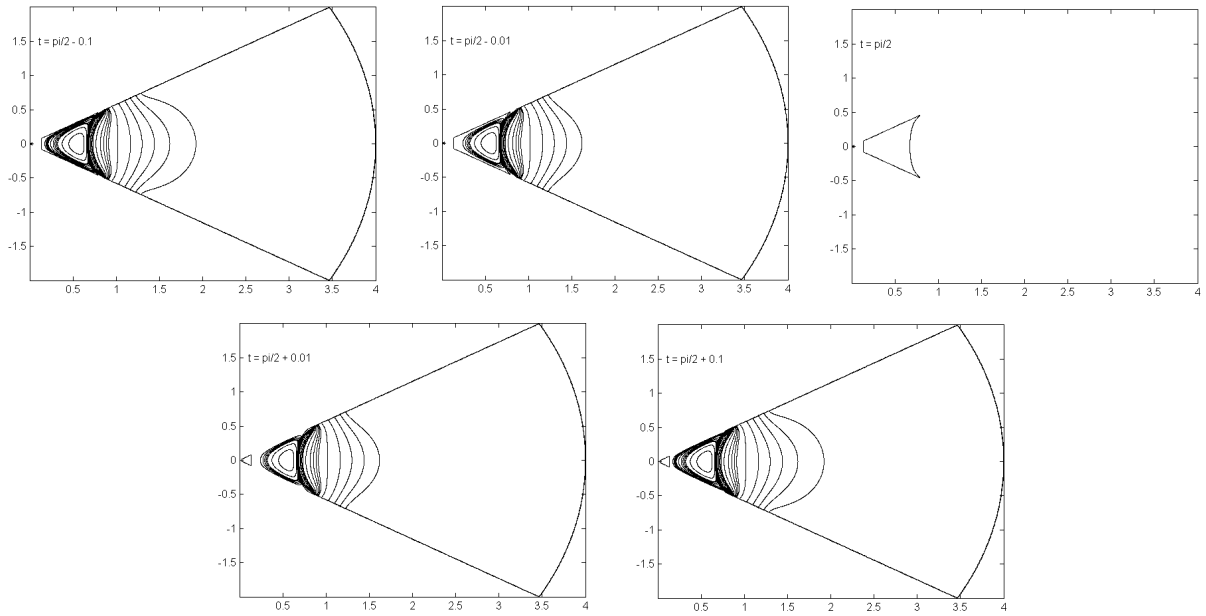

Figure I.4: Progressive sequence of contour plots for $(r,\theta,t) \longmapsto \hat{\psi}_0(r,\theta)\cos(t)$ near $t = \pi/2$

The addition of the $O(\eta)$ component induces enough lag within the fluid to allow us to witness the mechanism through which the flow reversal occurs. Indeed, we can observe that an eddy seems to be ejected from the corner, being extracted from the infinite sequence of eddies which existence was put to light in the previous paragraph.

This phenomenom is relatively intriguing and mind-challenging. One would not necesseraly expect a flow to have and infinite resevoir of eddies that can be discarded to trigger its reversal.

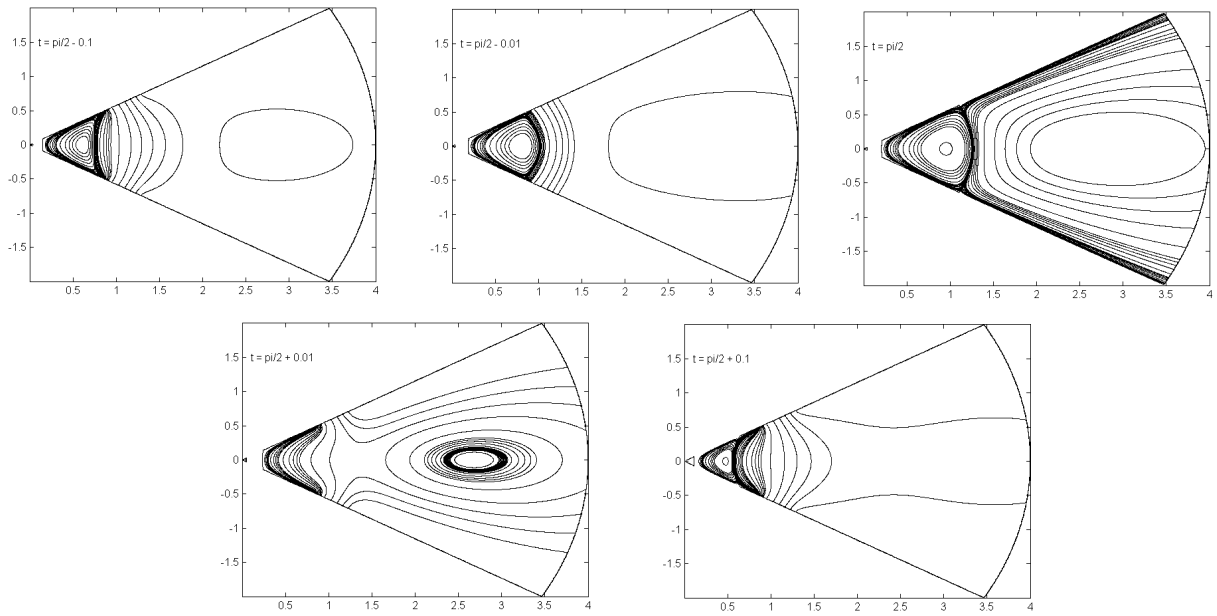

Figure I.5: Progressive sequence of contour plots for $(r,\theta,t) \longmapsto \hat{\psi}_0(r,\theta)\cos(t) - \eta\hat{\psi}_1(r,\theta)\sin(t)$ near $t = \pi/2$ for $\eta = 0.5$

Part II

Study of the dynamical system generated by the corner flow : mathematical approach and computations

Until now, this report presented the mathematical process used to obtain analytical solutions to simple yet general time-periodic corner flows problems as well as some of their key properties.

But let us now emphasize the principal aim of our work : we wish to quantify and analyse the mixing properties of the dynamical system describing the alveola. Doing this, we want to recover the local mixing properties exhibited by Messers Laine-Pearson and Hydon in [**?**] while developing and implementing a more general approach that would allow some further developments.

Hence, we need mathematical tools that will allow us to describe said properties and to represent them in a tangible form in order to understand how the dynamical system generated by our corner flow behaves and mixes. But first, let us shortly present the dynamical structure of our system.

II.1 Dynamical structure of the corner flow

The dynamical system seeded by the corner flow has the remarkable property of being Hamiltonian. Indeed, the mathematical relationship between the stream function ψ and the velocity field is the following

$$\frac{\mathrm{d}x}{\mathrm{d}t} = \frac{\partial \psi}{\partial y}(x,y,t) \quad , \quad \frac{\mathrm{d}y}{\mathrm{d}t} = -\frac{\partial \psi}{\partial x}(x,y,t) \quad \text{in Cartesian coordinates} \tag{II.1}$$

Determining the velocity fields of our system in the different cases will be rather easy. Indeed, we will only need to take the derivatives with respect to r and θ of the different expressions we displayed before in (I.21) or in the appendices. Moreover, since $v_x = \frac{\mathrm{d}x}{\mathrm{d}t}$ and $v_y = \frac{\mathrm{d}y}{\mathrm{d}t}$, the system has a Hamiltonian structure where ψ is the Hamiltonian.

II.2 Computational approach of the dynamical system properties

Now that we have mentionned briefly that our dynamical system has a particular structure, let us see what parameters and quantities will allow us to represent best its properties and whether this strong structure is affected by them. Note that the aim of this section is only to present in a concise and comprehensive way the numerical tools used to understand the system and to explain in more detail some of the difficulties encountered while doing so.

In the next subsections, we shall illustrate all our definitions using the case of a symmetric flapping boundary condition. This choice was made because it enables a simple representation of all the properties of interest we want to describe here.

- ◇ Finite Time Lyapunov Exponents :

  The *Finite Time Lyapunov Exponents* are a way to measure and describe the average stretching rate of a flow for $t \in [0,T]$ at any given point by looking at the evolution of trajectories which initial conditions are very close.

◇ Invariant Manifolds :

Invariant manifolds are geometric structures associated to hyperbolic trajectories. They represent particular trajectories along which the particles collapse exponentially on or diverge exponentially from an equilibrium.

Those structures yield insightful informations on the structure of a given system depending on their shape, their size, etc...

◇ Poincaré sections :

For time periodic dynamical systems with the extended phase space $(X,t) \in \mathbb{R}^n \times S^1_T$, where S^1_T is a circle of length T, Poincaré sections represent a map $X \mapsto X$ obtained from the flow map by $X_n = \phi_{nT}(X_0)$. It is a very powerful way of representing a periodic or quasi-periodic system, especially if its trajectories are bounded.

II.2.1 Finite Time Lyapunov Exponents

Definition

As mentioned before, the Finite Time Lyapunov Exponents (or FTLEs) are a simple way to give a first glance at the properties of a dynamical system. It yields a time average for the maximum expansion rate of two particles transported by the flow during a time t. A detailed definition of these exponents can be found in a lot of articles in the litterature. It is well and shortly defined in [7].

The FTLEs enable a first detection of some types of Lagrangian Structures (CLS), id est particular trajectories that have a predominant influence on nearby trajectories. In order to detect those structure, two types of FTLEs can be computed

- The forward FTLEs, which use forward time integration to reveal repelling CLS.
- The backward FTLEs, which use backward time integration to reveal attracting CLS.

Use of FTLEs

Even though these quantities may prove more than useful to grant a first look into the properties of a system, they suffer from being extremely sensitive to the total integration time T and the integration step δt. Indeed, depending on the system considered, changing those parameters may distort completely the picture obtained in the end. Thus, it is necessary to run the computations several times even though they may not seem eventually promising at first glance. Articles such as [8] deal with the limiting aspects of FTLEs.

Moreover, the best way to obtain information on the behaviour of the flow is to simultaneously plot the attracting and repelling manifolds. This way, it is possible to observe the points at which they are crossing and generating hyperbolic equilibriums. Identifying those equilibrium will then be of great use to compute invariant manifolds which are among the best mathematical objects for representing chaotic behaviours and transport properties of a system.

II.2.2 Invariant manifolds

Another way through which one can gain significant information about a dynamical system is the identification and computation of stable and unstable manifolds. These particular structures help one to identify barriers that particles will not be allowed to cross due to uniqueness of solutions as well as hyperbolic trajectories and motion trends.

Invariant manifolds can be of two types : stable manifolds which represent the points that will asymptotically collapse onto a given equilibrium and the unstable manifolds that represent the points which will diverge from it. Both collapse and divergence occur at an exponential rate.

Moreover, invariant manifolds should allow us to detect the presence of chaos depending on how the stable and unstable manifolds do twist and behave.

Remark. Invariant manifolds are necessarily associated to an equilibrium point, thus the need to try and identify them using FTLEs.

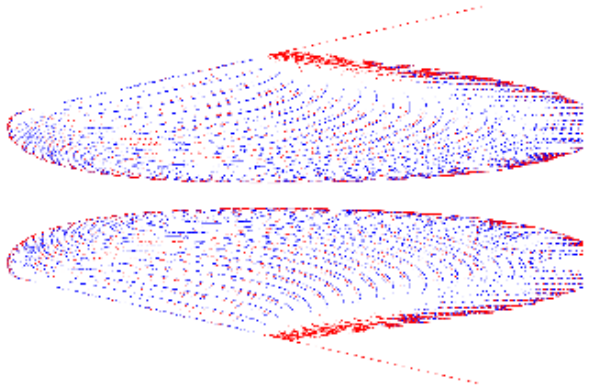

Figure II.1: Representation of both forward (blue) and backward (red) FTLEs

In our case, we shall plot these manifolds in the 2D-space (x, y). Since our system here is 2π-periodic in time, confining ourselves to $t \in [0, 2\pi]$ will be sufficient to describe the behaviour expected for $t \to \pm\infty$.

Examples of stable and unstable manifolds in the case of a symmetric flapping are shown in the figures II.2 and II.3.

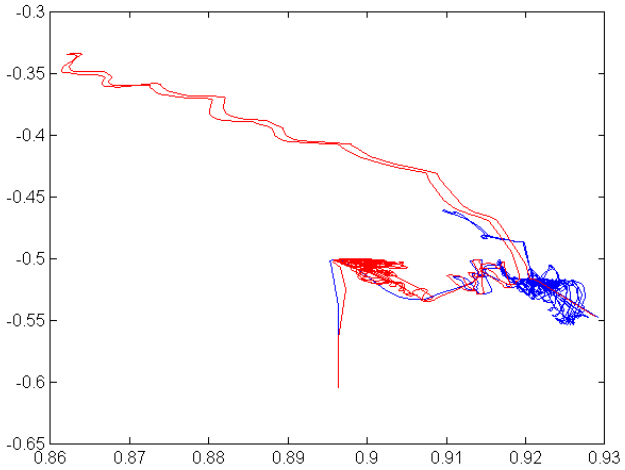

Figure II.2: Example of invariant manifolds with both the stable (blue) and the unstable (red) one seeded at $(x_e, y_e) \simeq (0.89, -0.56)$

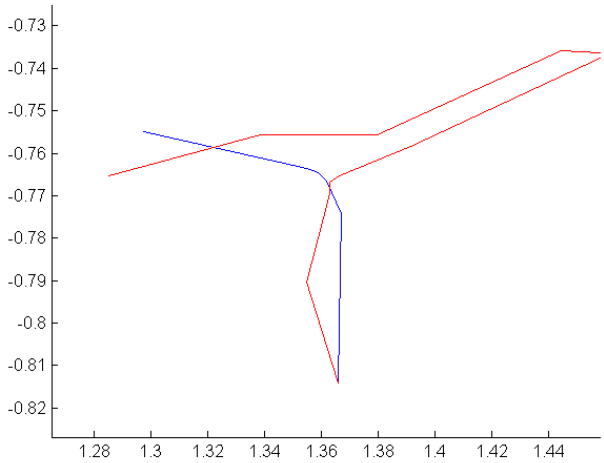

Figure II.3: Example of invariant manifolds with both the stable (blue) and the unstable (red) one seeded at $(x_e, y_e) \simeq (1.37, -0.81)$

Those structures yield powerful information on a system. Indeed, the invariant manifolds are barriers that particles cannot cross. Thus, depending on their shape and how they evolve with increasing time, it is possible to infer the existence or the absence of chaos and global transport. Moreover, the theoretical existence of chaos can be derived directly from them.

Indeed, a non-chaotic system will present non-oscillating invariant manifolds that do cross each other only at the equilibrium point(s) from which they are stemmed. In the case of a chaotic system, stable and unstable manifolds do oscillate and cross each other several times (see figure III.1 for example).

II.2.3 Poincaré sections

Poincaré section are often used to describe periodic or qiasi-periodic systems. They are maps representing the phase space of a system at regular time intervals.The figure II.4 shows an brief illustration of Poincaré sections where the (x_n) sequence corresponds to "snapchots" of the system's state x at regular time intervals.

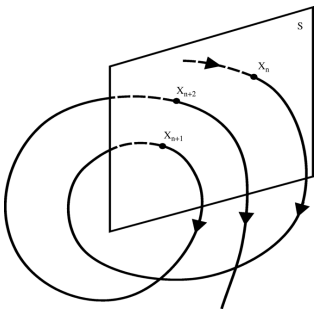

Figure II.4: Intuitive illustration of Poincaré sections in terms of phase space intersections

A more profound description of this mathematical tool can be found in a book dedicated to the study of dynamical systems.

Using Poincaré sections, it is fairly easy to see if a system is periodic, quasi periodic or chaotic. They give both quantitative and very interesting qualitative information on a system. Moreover, computing Poincaré sections enables the observer, for a sufficiently large number of points and periods, to witness the barriers that may exist within the system and observe which of those resist to chaos or shatter under its influence. Computing Poincaré sections is thus of high importance while studying a chaotic system, to account for both local mixing and global transport.

II.3 Structure of the main calculation codes : precision, robustness and performance

The quantities presented in the previous section where either computed on Matlab using codes I implemented myself or using a toolbox created by my Mr.Branicki a few years ago.

This section aims at presenting some of the numerical methods implemented and, importantly, what optimizations were to be made in the code in order to run them within decent time periods. Again, all the examples of pseudo-code will refer to the case of a symmetric boundary flapping problem. In this scope, let us describe briefly the numerical approaches we initially used to generate our stream functions and velocity fields in order to present afterwards the improvement we brought to it.

II.3.1 First computation of the velocity fields and stream functions

The very first step numerically speaking was to compute the spatial part of the stream function (given by (I.21) and (A)), the velocity fields derived from them (using (II.1)) and to plot them. Let it be reminded that in both cases, the spatial and time dependences are uncoupled.

This way, it was easy to check the consistency of our results and to verify whether the expressions we were going to use afterwards to compute FTLEs and manifolds were correct.

Furthermore, it was also a way to see in practice how the truncated series expansions behave and whether they achieve satisfactory approximations of the analytical solutions.

Basic computation approach concerning the stream functions

The approach we first followed to generate those functions was adapted from one Mr.Branicki previously implemented for a slightly different case. It was pretty much the most basic and intuitive one could follow since it was not requiring much optimization. The global procedure in the case of the $O(1)$ term was the following

- Set the desired number N of terms in series to a given value
- Compute/load the corresponding terms of the sequence $(p_m)_{1<m\leqslant N}$
- Generate three sets of polar coordinates (r_a,θ_a), (r_{ab},θ_{ab}) and (r_b,θ_b) corresponding to the three areas $r\leqslant 1$, $1\leqslant r\leqslant b$ and $r\geqslant b$ of the domain using the *meshgrid* function.
- Run a loop which evaluates the series expansions in (I.21) for each grid point and stores the results in three 3D array structures corresponding to the three areas of the domain.

- Apply a summation to the grids along their third dimension to obtain the truncated series expansions
- Evaluate separatly the non-series terms and add them to the truncated series expansions
- Merge the three parts of the stream function

This method has the pros of being simple and acceptably efficient for reasonable values of N. Moreover, it depends on two main parameters that characterise its calculation speed

- ◇ this method is in $O(N)$ when generating order 0-quantities and $O(N^2)$ for order 1-quantities.
- ◇ the arrays manipulated by the script are $m \times n \times N$ arrays where m and n depend on the area of the domain considered but are proportionate to the inverse of the radial grid size dr which is used to generate the discrete numerical coordinates r and θ.

From what precedes, it is possible to draw the conclusion that this method will, for reasonable N and dr values, be likely to be slow but however will not flood the RAM of the computer. Plus, the stream functions computed this way are smooth even for low values of N.

Concerning the velocity fields

The exact same computation approach was used to generate the velocity fields (after applying (II.1) to (I.21) and A), yielding the results displayed in figures II.5, II.6, II.7 and II.8

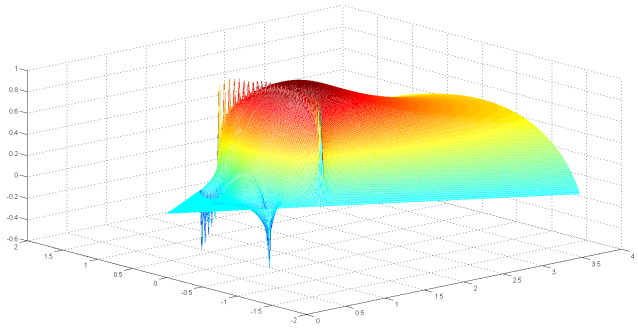

Figure II.5: Radial component of order 0the velocity in the case of a symmetric flapping for $N = 60$

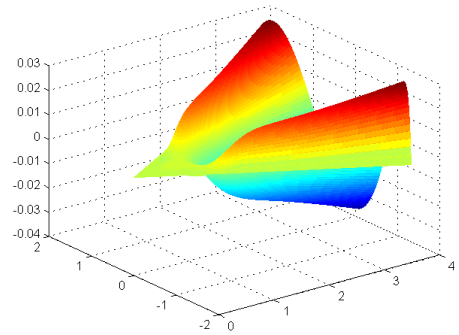

Figure II.6: Radial component of the order 1 velocity in the case of a symmetric flapping for $N = 60$

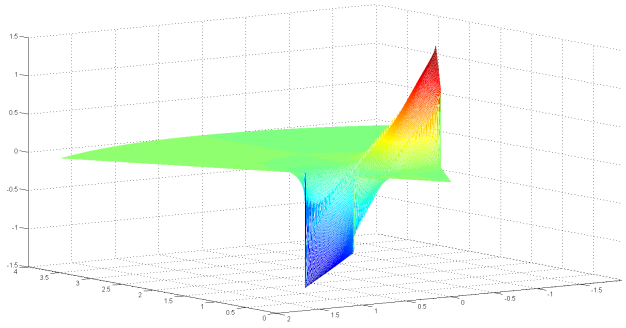

Figure II.7: Angular component of order 0the velocity in the case of a symmetric flapping for $N = 60$

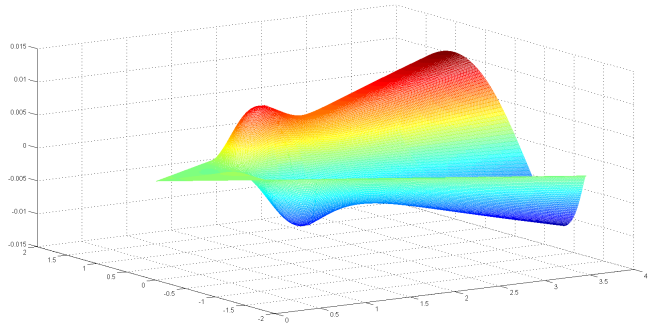

Figure II.8: Angular component of the order 1 velocity in the case of a symmetric flapping for $N = 60$

However, a couple of striking differences was observed in the course of performing the computations :

- The overall convergence with respect to the parameter N seems much slower than in the case of the stream functions, especially for the order 0 velocities.

- The order 0 velocities do not seem to converge at the interfaces as N grows.

The first remark is natural, since differentiating the stream function lowers the order of convergence with respect to N. A complete study of this convergence was made in the symmetric flapping case in Appendix D.3 where it is shown that because of this differentiation, the norm convergence we had for the stream function (see Appendix D.1) does not hold anymore.

The second phenomenom, which unlike the first one was not at all expected, can be explained by the lack of robustness of our solutions with respect to numerical errors made on the p_ms. This particular point is elaborated upon in the Appendix D.4.

II.3.2 Implementation in the frame of the main computing scripts

Once we managed to compute and plot the stream functions and the velocities, the next step was to use them to compute FTLEs, manifolds, and Poincaré sections. The main idea behind these computations was roughly similar in each case : the velocity field was numerically integrated in time (most of time using a fourth-order Runge Kutta method) in order to obtain trajectories which were then the primary blocks used to generate the other quantities. However, these computations were mainly effected using two different approaches :

- ◇ The FTLEs and manifolds computation is based on the same idea as the code generating stream functions. The toolbox generates Cartesian coordinate grids to which the velocity functions are applied in order to represent those quantities within the whole domain or part of it. It can be seen as a fieldwise representation of the velocities and stream functions.
- ◇ The computation of Poincaré sections is much more of a pointwise iterative process. The velocity functions are applied to a set of single initial conditions and the spatial coordinates are modified at each and every iteration.

These two distinct numerical approaches called for different needs in terms of computational optimization which we shall explain separately next.

Optimization of the manifolds and FTLEs computation codes

As mentioned before, the main principle of these codes is to evaluate the whole velocity field on a Cartesian grid whose size is fixed by the user and that will define the spatial accuracy of the plotted quantities. Therefore, the main idea behind this code is the same as the one presented afore for the stream functions and the velociy fields.

These codes were available in the matlab toolbox I used. Therefore, I did not implement them and do not know precisely how they work. However, I had to go through several code modifications for them to fit the toolbox format and had to change their structure several times in order to make them more efficient.

Two main issues were to be dealt with in that scope : the non-smooth character of the velocity fields and the non-optimality of our first code.

Getting rid of the loop structure The numerical integration used to compute manifolds and FTLEs could be in certain cases rather voluminous, with for instance integration loop sometimes running over a few hundreds of thousands of steps. Thus, the loop-based structure presented hereabove to compute the spatial part of the velocity fields was to be avoided for any computation to take a reasonable time. Two options presented themselves to speed this up in a simple way :

1. The first one was to get rid of the loops by generating 3D meshgrid structures for the spatial variables r and θ as well as for the $(p_m)_{1<m\leqslant N}$. This way, it was possible (with some slight modifications in the code and extra care) to do all the computation using 3D-arrays to which the velocity formulas could be applied. This kind of structure is much more efficient with Matlab, but is however less efficient than the following one which we chose.
2. The idea we followed was to generate the spatial component of both stream functions and velocity fields beforehand using the method described in (II.3.1) and to store them in lookup tables. These tables would then be defined as persistent variables, called whenever necessary and interpolated on the running grid.

This last method prooved to be very efficient. Moreover, it enabled us to deal once and for all in a perfectly controlled way with the other main numerical issue concerning those computations : the non-convergence of the order 0 velocities at the interfaces $r = 1$ and $r = b$.

Smoothing the velocity fields As shown in the previous sections and in Appendix D, the series expansions involved in the order 0 velocity fields did not seem to converge at the interfaces $r = 1$ and $r = b$ with N increasing. Furthermore, this error could apparently not be alleviated, even by grouping terms within the calculations or by refining the tolerance and accuracy parameters of the zero-finding function evaluating the p_ms. And as a matter of fact, having a highly discontinuous velocity or a velocity which derivatives are discontinuous would be disastrous in our case since we want to integrate it in order to obtain trajectories.

Different fruitless but very instructive approaches were first experimented to try and remove this numerical issues

1. Our first attempt before identifying the source of the problem was to approximate the velocity field by a finite-differences method directly from the stream function. This however resulted in the very same result.

2. We then tried to increase the precision of the computation of the $(p_m)_{1<m\leqslant N}$ values (see appendix D.21 for more precision). We tried to make the real and imaginary parts of the W function steeper near its zeros by taking its modulus and elevating it to a small fractional power. This should theoretically have improved the convergence of the zero-finding procedure calculating them, but it did not work.

3. Lastly, we tried to smooth the arrays containing the velocity values along the interfaces using spatial arithmetical averaging with suitable coefficents.

Even though the last proposition might seem relevant, it did not preserve the angular smoothness of the functions along the interfaces and brought some discontinuities. We finally chose, in order to fix the problem while denaturing the least possible our solution, to use convolution products with Gaussian kernels.

The only drawback of this method was to slightly crop our solutions on the boundaries by including out of domain terms because of the spatial averaging. However, it yielded results that were more than satisfactory with regard to all the other aspects mentioned before (smoothness, preservation of the global characteristics of the solutions, etc...).

II.3.3 Structure and optimization of the Poincaré section computation code

Unlike the FTLEs and manifolds computing for which I mainly had to adapt and modify my code to an existing structure, this one I had to implement from scratch and figure out how to improve its performance.

The main idea of the code here is to integrate numerically the system of non-linear differential equations defined by (II.1) and to plot the points corresponding to times that are integral multiples of 2π. Unlike the codes presented before, Poincaré sections computation does not allow us to separate completely the spatial and temporal components of the velocity, or at least not in a simple way.

To do so, we had to re-use the same code structure as the one described in (II.3.1) that generates the velocity fields but in the frame of a numerical integrating scheme where the inputs (r,θ) were scalars and not arrays. I managed to get rid of the loops within the code computing those fields by applying all the calculations to arrays containing the p_m values.

I first started by using the Matlab solver *ode45*, which however presented some serious drawbacks :

1. This integrating scheme being time step-adaptative, it was bound to be relatively slow. Plus, we saw that the series expansions involved in the velocity fields did not converge numerically at the order 0. This issue we managed to remedy by smoothing the spatial components of the velocity when computing FTLEs and manifolds, but it was not possible to do the same here. The velocities are thus bound to be discontinous or to have discontinuous derivatives, which would make a time step - adaptative method even slower.

2. Furthermore, in some cases, we had to impose constraints on the integration scheme. For instance, we had to numerically mimick the existence of the oscillating wall of the alveola and make sure that particles were not crossing it. This type of discrimination can be notably difficult to take into account in a general way using Matlab solvers such as *ode45*.

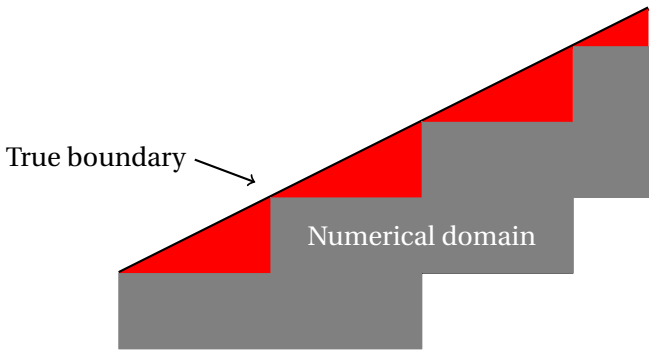

Figure II.9: Illustration of the interpolation inconsistency arising on the numerical boundary of the domain

Because of those two reasons, we chose to use a fourth-order Runge Kutta method which is very simple to implement, conveniently fast and easily customizable when it comes to adding constraints.

Moreover, a quick comparison between the two methods showed that this simpler scheme approximated rather well the solutions of the Matlab solver *ode45* if the fixed time step was reasonnably small.

II.4 Interpolation inconsistency arising on the boundary

After having developped these tools and coded their computation scripts, we were hoping to use them to describe accuratly the chaotic properties of our system. However, late into our work, a major computation flaw arose in the codes concerning the invariant manifolds and FLTEs.

This difficulty, which we already had to deal with to a lesser degree for the Poincaré sections script, is that numerically, the trajectories are necessarily discrete. Thus, when particles are dragged to the boundary where the forcing occurs, they can very well cross the "imaginary" barrier of the domain. Since the solutions do not hold outside of the wedge, this situation can lead to two different yet equally problematic outcomes :

- If the velocity outside the wedge is manually put to zero, the particles wandering there are then blocked on false equilibriums.

- If not, the trajectories tend to diverge from the wedge and go to infinity.

The computations of FTLEs, manifolds, and Poincaré sections all require integrating the velocity field. However, as it is mentioned earlier in this chapter, Poincaré sections are computed pointwisely and the velocity at any given point is calculated for each step. On the other hand, the computation of FTLEs and manifolds uses the whole grid of velocities.

In each case, this grid is first generated in a polar coordinates setup and then interpolated on a cartesian grid. Even though it did not occur to us initially, this interpolation was bound to flaw our results. Indeed, it did lead to a numerical deformation of the boundary and then to a loss of consistency by zeroing the velocity where it should have been non-zero as illustrated in figure II.9 .

The areas coloured in red on figure II.9 are portions of the true domain that do not appear in the numerical one and that are thus considered to have a velocity identically equal to zero.

Since manifolds and FTLEs are drawn based on the motion of particles, this error has the effect of transforming the major part of the boundary into a zero-velocity area and thus into a serie of equilibrium points. Since the boundary within the forcing area clearly has non-zero velocity components, this error affects the whole behaviour of the fluid.

Hereafter follows a quick example of FTLEs in the case where one coarsens the lookup tables by taking one every five points. It is then easier to spot the inconsistency described earlier.

We thought about several possibilites to fix this problem that is bound to happen whenever a flapping boundary motion is involved :

- First, we could monitor the motion of the flapping boundary in order to make sure that particles can wander outside the geometric limits of the wedge in the forcing area while remaining within its "physical" boundaries.

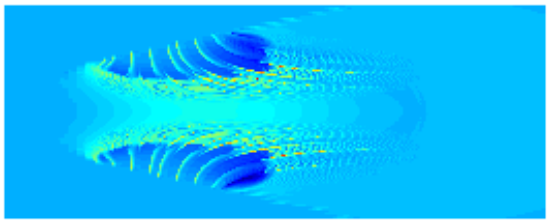

Figure II.10: Illustration of the boundary inconsistency in the case of forward FTLEs

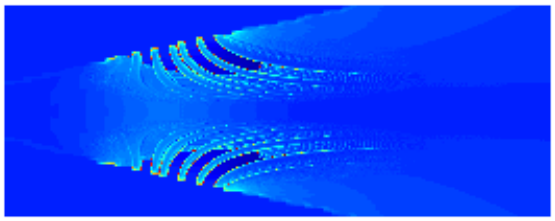

Figure II.11: Illustration of the boundary inconsistency in the case of backward FTLEs

- Another option would be to make sure that particles do not stick to the boundary, possibly by pulling them apart from it whenever the flapping motion changes sign.

Whichever solution we choose, it will be implemented in the scope of a forthcoming artcile we are currently working on but was not available in time for this report.

Part III

Practical analysis of different flapping cases and work in progress

Even though some of our codes will not be able to deliver ideal results alongside with profound and perfect phenomenom explanations, we are still able to describe to a lesser degree some of the observed behaviours and to recover partly the properties we were seeking.

III.1 Analysis of the symmetric flapping case

Let us focus now on the case of the symmetric flapping. The FTLEs corresponding to this case have already been displayed within this report to illustrate the different tools we introduced in chapter II.Even though they suffer from the numerical errors mentioned in II.4, they enable us to witness the existence of an invariant for $\theta = 0$.

Moreover, they enable us to infer the existence of hyperbolic trajectories on the boundaries. Sadly, unlike the FTLEs plottings, the manifolds do really suffer from this inconsistency and are not exploitable at the moment. The behaviour we are hoping to observe once the code will be properly fixed is the following.

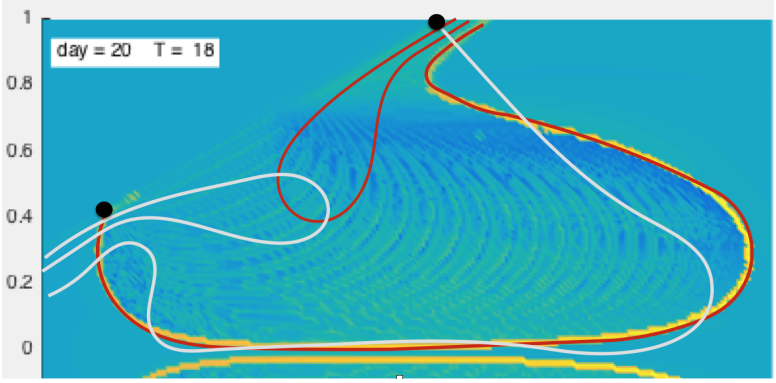

Figure III.1: A guess for the unstable (red) and the stable (gray) manifolds

The fact that those manifolds twist even at the $O(1)$ order is a sign that there exists chaos. What would be interesting and what we would hope to see upon including the $O(\eta)$ component would be a sharp increase of the number of lobes and of their size which would describe global transport behaviour and an increase of local chaos.

The only practical expression of those expectancies we managed to obtain is contained in the plotting of Poincaré sections in figures III.4, III.5, III.6 and III.7 and partly of the FTLEs in figures III.2 and III.3.

Indeed, the ridges observed upon coarsening the lookup tables in the FTLEs are notably longer at the same time t and for the same integration parameters T and δt when the $O(\eta)$ term is added (see figures III.2 and III.3). This denotes the fact that particles comprised within those invariants are given more space to travel inside the wedge.

On the other hand, the computation of Poincaré sections yields interesting information concerning the effect of the $O(\eta)$ component as well. As it can be seen in the figures III.5 and III.7, the $O(\eta)$ term seems to break some of the barriers existing in the case where only the $O(1)$ is present since particles are experiencing global transport

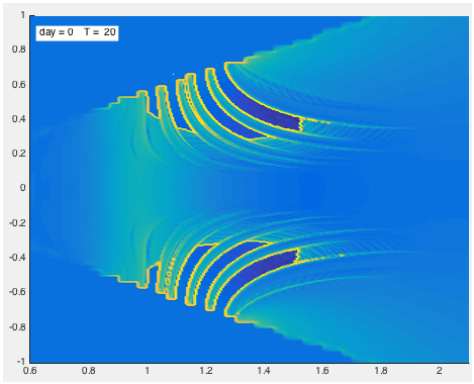

Figure III.2: Forward FTLEs for the order 0 symmetric flapping using coarsened lookup tables

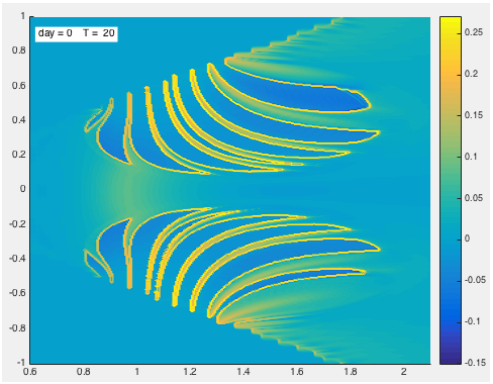

Figure III.3: Forward FTLEs for the order 1 symmetric flapping using coarsened lookup tables

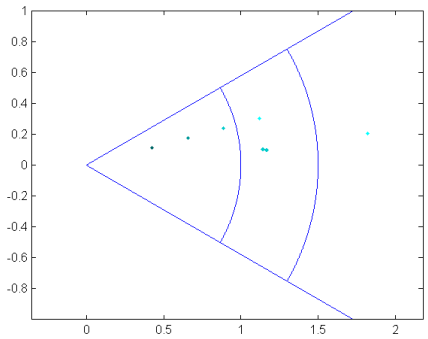

Figure III.4: Poincaré sections including only the order 0 velocity in the symmetric flapping case

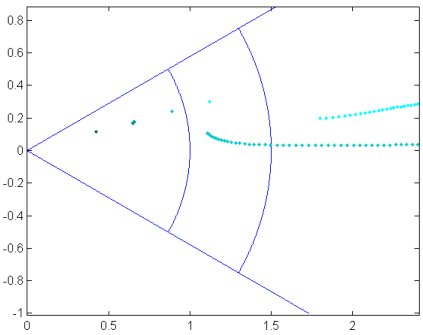

Figure III.5: Poincaré sections including only the order 1 velocity in the symmetric flapping case for $\eta = 0.8$

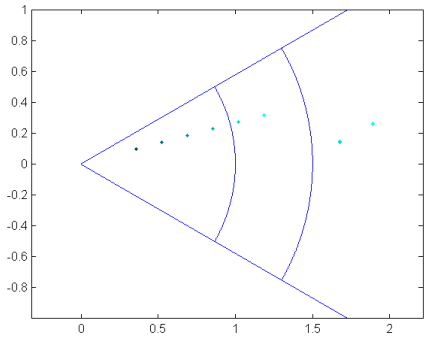

Figure III.6: Poincaré sections including only the order 0 velocity in the symmetric flapping case

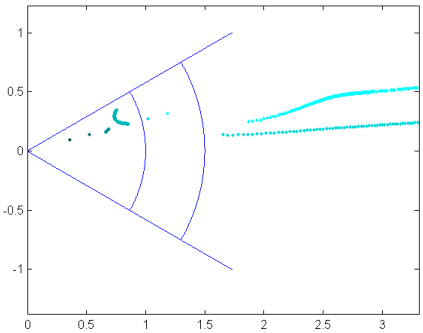

Figure III.7: Poincaré sections including only the order 1 velocity in the symmetric flapping case for $\eta = 0.8$

in a very visible way. Plus, some local chaos can be witnessed notably in figure III.4. However, the effect of the $O(\eta)$ is rapidly negligible when r decreases. This is consistent with the fact that the Stokes flow approximation gets stronger near the corner where the flow is highly viscous.

III.2 Overtures and coming progresses

Even though we did not manage to extract all the information our two canonical cases could yield, the fact that we have at our disposal the analytical expressions of the solutions will allow us to easily generate more interesting cases.

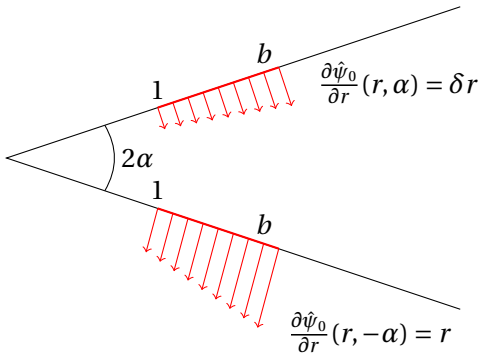

Figure III.8: Illustration of a general flapping boundary motion

III.2.1 General periodic motion

An easy way to generalize a bit further our approach while remaining in a time-periodic frame is to assume that the two sides of the wedge where the forcing is non zero have motions of different amplitudes.

Let us assume that, before non-dimensionalizing our problem, the boundary region corresponding to $(r,\theta)\in[1,b]\times\{\alpha\}$ is subjected to the periodic velocity forcing $\mathcal{U}_1(r,t)=r\hat{U}_1\cos(\omega t)$ and $(r,\theta)\in[1,b]\times\{-\alpha\}$ to $\mathcal{U}_2(r,t)=r\hat{U}_2\cos(\omega t)$.

The non dimensionalizing velocity parameter will be the largest of two amplitudes in absolute value. Let us assume for instance that $|\hat{U}_2|\leqslant|\hat{U}_1|$. Once refined as it was done in section (I.1) and put in the same form as (I.10), this generalized flapping problem can be written :

$$\begin{cases} \nabla^4\hat{\psi}_0=0 \quad \text{in } \mathcal{D} \\ \dfrac{1}{r}\dfrac{\partial\hat{\psi}_0}{\partial\theta}=0 \quad \text{on } \theta=\pm\alpha \\ \dfrac{\partial\hat{\psi}_0}{\partial r}=\begin{cases} 0 \text{ if } r<1 \\ r \text{ if } 1<r<b \ , \ \theta=\alpha \\ \delta r \text{ if } 1<r<b \ , \ \theta=-\alpha \\ 0 \text{ if } r>b \end{cases} \end{cases} , \quad \begin{cases} \nabla^4\hat{\psi}_1-i\eta\nabla^2\hat{\psi}_0=0 \quad \text{inside } \mathcal{D} \\ \dfrac{\partial\hat{\psi}_1}{\partial r}=\dfrac{1}{r}\dfrac{\partial\hat{\psi}_1}{\partial\theta}=0 \quad \text{on } \theta=\pm\alpha \end{cases} \tag{III.1}$$

where $\delta=U_2/U_1$ can be either positive or negative as long as the prerequisites necessary to the asymptotic expansions are met.

A short focus on the boundary conditions affecting $\frac{\partial\hat{\psi}_0}{\partial r}$ is now necessary. For convenience, the boundary conditions describing both a symmetric and an skew-symmetric flapping motion are recalled hereafter :

$\frac{\partial\hat{\psi}_0^{\text{sym}}}{\partial r}(\pm\alpha)=\pm r$ in the symmetric case and $\frac{\partial\hat{\psi}_0^{\text{asy}}}{\partial r}(\pm\alpha)=r$ in the skew-symmetric one.

It can thus be easily seen that the corresponding boundary conditions described in III.1 can be obtained by taking

$$\hat{\psi}_0(r,\theta)=\frac{(1-\delta)}{2}\hat{\psi}_0^{\text{sym}}(r,\theta)+\frac{(1+\delta)}{2}\hat{\psi}_0^{\text{asy}}(r,\theta) \tag{III.2}$$

Hence, it is possible to obtain the solution of a very general flapping boundary-problem by simply taking a linear combination of the solutions of the two canonical symmetric and skew-symmetric problems with coefficients depending only on the ratio of the two velocity amplitudes δ. This type of configuration is illustrated in figure III.8.

Remark. The method detailed hereabove can be applied to create a general tangential motion or even more complicated motions that will be combinations of tangential and normal oscillations. The exact same kind of structure of the solution is going to appear, taking the form of linear combinaitions depending solely on parameters δ_k symbolizing the different amplitude ratios.

III.2.2 Combination of elementary solutions of different periodicities

In the most general case, one would not necessary expect the function describing the boundary motion to have a simple 2π time-periodic behaviour or even to be time-periodic at all. A simple way to design a solution

have either a more complicated periodic behaviour or an aperiodic one is to combine a given number of time periodic motions of incommensurate periods. We next explain this procedure in the simple case of two solutions.

Let us define two general boundary motions $\mathcal{U}_1(r,t)$ and $\mathcal{U}_2(r,t)$ of periods ω_1 and ω_2 and of equal amplitudes. Let it be assumed that we non-dimensionalize the time variable with respect to ω_1 (for instance).

The solution to the problem corresponding to the boundary condition $\mathcal{U}(r,t) = \mathcal{U}_1(r,t) + \mathcal{U}_2(r,t)$ will then take the following form in keeping with the notations introduced in (I.1.2)

$$\psi_0^{(u)}(x,y,t) = \mathcal{R}\left[e^{it}\left(\hat{\psi}_0^1(x,y) + i\eta_1\hat{\psi}_1^1(x,y)\right)\right] + \mathcal{R}\left[e^{\frac{\eta_2}{\eta_1}it}\left(\hat{\psi}_0^2(x,y) + i\eta_2\hat{\psi}_1^2(x,y)\right)\right] \tag{III.3}$$

This can be easily verified using the equations in (I.7) and remarking that $\eta_2/\eta_1 = \omega_2/\omega_1$. We then have a solution which is a linear combination of the solutions to the two boundary forcings $\mathcal{U}_1$ and $\mathcal{U}_2$ and which coefficients depend only on the period ratio η_2/η_1.

Conclusion

During this research internship, we solved several different wedge flow problems in order to be able to create more complex behaviour for our wedge dynamic. We managed to convey a complete analysis of our solutions and to dissect the diverse mathematical and computational features arising from them. The next step in our work will be now to use those primary blocks to generate behaviour that could be physically accurate to describe a pulmonar alveola.

Even though we did not obtain perfecly exploitable results, we identified the causes of inconsistencies and explained how they triggered some of the odd behaviours we observed. And even considering those errors, it was possible to partly explain how our model seemed more relevant on several aspect. Besides, we saw how adding the $O(\eta)$ corrective term should trigger global transport in some areas of the domain as well as an increase of local chaos and mixing.

Our approach proved to be mathematically more general. Indeed, it did not require the strong hypothesis of the system being nearly-integrable. Moreover, it also leads to more profound explanations of phenomena arising within the flow that do not concern mixing such as the existence of sequences of eddies that trigger the flow reversal.

We are still working Mr.Branicki and I on the different codes in order to be able to simulate more complex behaviour that we could describe explicitly using FTLEs, manifolds and Poincaré sections, towards eventually publishing an article. We wish in particular to accurately study the cases of aperiodic flows or flows that are created as a superimposition of normal and tangential boundary motions.

In terms of personal outcomes, I learned a lot from this experience. I am very motivated by the idea of continuing to work on this topic and exploring the different aspects of this class of problems. I particularly liked the notion of having a very wide subject which I could explore in different directions depending on what intrigued me or what was necessary at the moment. I worked in a rather free and autonomous fashion which did suit me and motivated me a lot.

Lastly, I would like to thank again Mr.Branicki for his support and his motivational attitude. I am very grateful for the opportunity of working on a real research topic that will hopefully lead to a publication.

Appendix A

Order 1 component of the solution to a normal and symmetric boundary forcing problem

The analytical solution for the $O(\eta)$ correction to the Stokes flow approximation driven by flapping boundary conditions inside an infinite wedge is given below in the three distinct regions $r \leqslant 1$, $1 \leqslant r \leqslant b$, $r \geqslant b$.

For $r \leqslant 1$, the solution takes the following form :

$$
\begin{aligned}
\hat{\psi}_1(r,\theta) =& 4i \sum_{m<-1} \frac{Z(b^{p_m+4}-1)\cos(2\alpha)}{W'(p_m)p_m^2(p_m+2)^2(p_m+4)r^{p_m}}\left[-\Omega(p_m+2)\sin(p_m\theta)+\Omega(p_m)\sin[(p_m+2)\theta]\right] \\
& 2i \sum_{m<-1} \frac{Z(b^{p_m+4}-1)}{W'(p_m)p_m(p_m-2)(p_m+2)^2(p_m+4)r^{p_m}}\left(\mathcal{U}_2(p_m)\sin(p_m\theta)+\mathcal{V}_2(p_m)\sin[(p_m+2)\theta]\right) \\
& -4i \sum_{n>1} \Bigg[X_n(b^{2-p_n}-1)\frac{\mathcal{U}'_{p_n}(-p_n-2)\sin[(p_n+2)\theta]+\left[\mathcal{V}'_{p_n}(-p_n-2)-W'(-p_n-2)\right]\sin(p_n\theta)}{16W'(-p_n-2)p_n(p_n+1)r^{-p_n-2}} \\
& \quad - X_n(b^{-p_n}-1)\frac{\mathcal{U}_{p_n}(-p_n-4)\sin[(p_n+4)\theta]+\mathcal{V}_{p_n}(-p_n-4)\sin[(p_n+2)\theta]-W(-p_n-4)\sin(p_n\theta)}{32W(-p_n-4)(p_n+1)(p_n+2)r^{-p_n-4}} \\
& \quad + X_n \sum_{\substack{m<-1 \\ m\neq -n}} (b^{p_m+4}-1)\frac{\mathcal{U}_{p_n}(p_m)\sin(p_m\theta)+\mathcal{V}_{p_n}(p_m)\sin[(p_m+2)\theta]}{W'(p_m)(p_m+p_n+4)(p_m-p_n)(p_m+p_n)(p_m+p_n+2)(p_m-p_n+2)r^{p_m}} \Bigg] \\
& +4i \sum_{n>1} \Bigg[Y_n(b^{2-p_n}-1)\frac{\mathcal{V}'_{p_n+2}(-p_n-2)\sin(p_n\theta)+\left[\mathcal{U}'_{p_n+2}(-p_n-2)-W'(-p_n-2)\right]\sin[(p_n+2)\theta]}{16W'(-p_n-2)p_n(p_n+1)r^{-p_n-2}} \\
& \quad + Y_n \sum_{\substack{m<-1 \\ m\neq -n}} (b^{p_m+4}-1)\frac{\mathcal{U}_{p_n+2}(p_m)\sin(p_m\theta)+\mathcal{V}_{p_n+2}(p_m)\sin[(p_m+2)\theta]}{W'(p_m)(p_m+p_n+4)(p_m-p_n)(p_m-p_n-2)(p_m+p_n+2)(p_m-p_n+2)r^{p_m}} \Bigg]
\end{aligned}
\tag{A.1}
$$

Same, for $b \leqslant r$, the solution is given by :

$$
\begin{aligned}
\hat{\psi}_1(r,\theta) = -4i \sum_{m<-1} & \frac{Z(b^{p_m+4}-1)\cos(2\alpha)}{W'(p_m)p_m^2(p_m+2)^2(p_m+4)r^{p_m}}\left[-\Omega(p_m+2)\sin(p_m\theta)+\Omega(p_m)\sin[(p_m+2)\theta]\right] \\
& -2i \sum_{m<-1} \frac{Z(b^{p_m+4}-1}{W'(p_m)p_m(p_m-2)(p_m+2)^2(p_m+4)r^{p_m}}\left(\mathcal{U}_2(p_m)\sin(p_m\theta)+\mathcal{V}_2(p_m)\sin[(p_m+2)\theta]\right) \\
& +4i \sum_{n>1}\Bigg[X_n(b^{2-p_n}-1)\frac{\mathcal{U}'_{p_n}(-p_n-2)\sin[(p_n+2)\theta]+\left[\mathcal{V}'_{p_n}(-p_n-2)-W'(-p_n-2)\right]\sin(p_n\theta)}{16W'(-p_n-2)p_n(p_n+1)r^{-p_n-2}} \\
& \quad + X_n \sum_{\substack{m<-1\\ m\neq -n}} (b^{p_m+4}-1)\frac{\mathcal{U}_{p_n}(p_m)\sin(p_m\theta)+\mathcal{V}_{p_n}(p_m)\sin[(p_m+2)\theta]}{W'(p_m+p_n+4)(p_m-p_n)(p_m+p_n)(p_m+p_n+2)(p_m-p_n+2)r^{p_m}}\Bigg] \\
& +4i \sum_{n>1}\Bigg[Y_n(b^{2-p_n}-1)\frac{\mathcal{V}'_{p_n+2}(-p_n-2)\sin(p_n\theta)+\left[\mathcal{U}'_{p_n+2}(-p_n-2)-W'(-p_n-2)\right]\sin[(p_n+2)\theta]}{16W'(-p_n-2)p_n(p_n+1)r^{-p_n-2}} \\
& \quad + Y_n(b^{p_n+2}-1)\frac{\mathcal{U}_{p_m+2}(p_m-2)\sin[(p_m-2)\theta]+\mathcal{V}_{p_m+2}(p_m-2)\sin[p_m\theta]+W(p_m-2)\sin[(p_m+2)\theta]}{32W(p_m-2)p_m(p_m+1)r^{p_m-2}} \\
& \quad + Y_n \sum_{\substack{m<-1\\ m\neq -n}} (b^{p_m+4}-1)\frac{\mathcal{U}_{p_n+2}(p_m)\sin(p_m\theta)+\mathcal{V}_{p_n+2}(p_m)\sin[(p_m+2)\theta]}{W'(p_m)(p_m+p_n+4)(p_m-p_n)(p_m-p_n-2)(p_m+p_n+2)(p_m-p_n+2)r^{p_m}}\Bigg] \\
& +\frac{i(b^2-1)Zr^2}{8[\sin(\alpha)-2\alpha\cos(2\alpha)]}\left[\mathcal{V}'_2(-2)\theta+\mathcal{U}'_2(-2)\theta\cos(2\theta)+\frac{1}{2}W''(-2)\sin(2\theta)\right]
\end{aligned}
\tag{A.2}
$$

Similarly, for $1 \leqslant r \leqslant b$ the solution is given by :

$$
\begin{aligned}
\hat{\psi}_1(r,\theta) =& 4i \sum_{|m|>1} \frac{Z c_m^{p_m+4} \cos(2\alpha)}{W'(p_m) p_m^2 (p_m+2)^2 (p_m+4) r^{p_m}} \left[-\Omega(p_m+2)\sin(p_m\theta) + \Omega(p_m)\sin[(p_m+2)\theta] \right] \\
& 2i \sum_{|m|>1} \frac{Z c_m^{p_m+4}}{W'(p_m) p_m (p_m-2)(p_m+2)^2 (p_m+4) r^{p_m}} \left(\mathcal{U}_2(p_m)\sin(p_m\theta) + \mathcal{V}_2(p_m)\sin[(p_m+2)\theta] \right) \\
& -4i \sum_{n>1} \left[X_n b^{2-p_n} \frac{\mathcal{U}'_{p_n}(-p_n-2)\sin[(p_n+2)\theta] + \left[\mathcal{V}'_{p_n}(-p_n-2) - W'(-p_n-2) \right] \sin(p_n\theta)}{16 W'(-p_n-2) p_n (p_n+1) r^{-p_n-2}} \right. \\
& \quad - X_n b^{-p_n} \frac{\mathcal{U}_{p_n}(-p_n-4)\sin[(p_n+4)\theta] + \mathcal{V}_{p_n}(-p_n-4)\sin[(p_n+2)\theta] - W(-p_n-4)\sin(p_n\theta)}{32 W(-p_n-4)(p_n+1)(p_n+2) r^{-p_n-4}} \\
& \quad + X_n \frac{[\mathcal{U}'_{p_n}(p_n) + W'(p_n)]\sin(p_n\theta) + \mathcal{V}'_{p_n}(p_n)\sin[(p_n+2)\theta]}{16 W'(p_n) p_n (p_n+1)(p_n+2) r^{p_n}} \\
& \quad \left. + X_n \sum_{\substack{|m|>1 \\ |m|\neq n}} c_m^{p_m+4} \frac{\mathcal{U}_{p_n}(p_m)\sin(p_m\theta) + \mathcal{V}_{p_n}(p_m)\sin[(p_m+2)\theta]}{W'(p_m)(p_m+p_n+4)(p_m-p_n)(p_m+p_n)(p_m+p_n+2)(p_m-p_n+2) r^{p_m}} \right] \\
& +4i \sum_{n>1} \left[Y_n b^{2-p_n} \frac{\mathcal{V}'_{p_n+2}(-p_n-2)\sin(p_n\theta) + \left[\mathcal{U}'_{p_n+2}(-p_n-2) - W'(-p_n-2) \right] \sin[(p_n+2)\theta]}{16 W'(-p_n-2) p_n (p_n+1) r^{-p_n-2}} \right. \\
& \quad - Y_n \frac{\mathcal{U}_{p_n+2}(p_n)\sin(p_n\theta) + [W'(p_n) + \mathcal{V}_{p_n+2}(p_n)]\sin[(p_n+2)\theta]}{16 W'(p_n)(p_n+1)(p_n+2) r^{p_n}} \\
& \quad + Y_n \frac{\mathcal{U}_{p_m+2}(p_m-2)\sin[(p_m-2)\theta] + \mathcal{V}_{p_m+2}(p_m-2)\sin[p_m\theta] + W(p_m-2)\sin[(p_m+2)\theta]}{32 W(p_m-2) p_m (p_m+1) r^{p_m-2}} \\
& \quad \left. + Y_n \sum_{\substack{|m|>1 \\ |m|\neq n}} c^{p_m+4} \frac{\mathcal{U}_{p_n+2}(p_m)\sin(p_m\theta) + \mathcal{V}_{p_n+2}(p_m)\sin[(p_m+2)\theta]}{W'(p_m)(p_m+p_n+4)(p_m-p_n)(p_m-p_n-2)(p_m+p_n+2)(p_m-p_n+2) r^{p_m}} \right] \\
& + \frac{iZ\cos(2\alpha) r^4}{16 W(-4)} \left[-W(-4)\theta - \Omega(2)\sin(4\theta) + \Omega(4)\sin(2\theta) \right] \\
& + \frac{i r^2}{8\left[\sin(2\alpha) - 2\alpha\cos(2\alpha)\right]} \left[\mathcal{V}'_2(-2)\theta + \mathcal{U}'_2(-2)\theta\cos(2\theta) + \frac{1}{2} W''(-2)\sin(2\theta) \right]
\end{aligned}
\tag{A.3}
$$

where : $c_m = \begin{cases} 1 & \text{if } m > 1 \\ b & \text{if } m < 1 \end{cases}$ and where the different functions and coefficients X_n , Y_n , Z , $W(\bullet)$, $\mathcal{U}_\bullet(\bullet)$, $\mathcal{V}_\bullet(\bullet)$ and $\Omega(\bullet)$ are given by (I.28) and (I.27) and where $f'(x) = \frac{\mathrm{d}f}{\mathrm{d}x}(x)$.

Appendix B

Full solution to a normal and skew-symmetric boundary forcing problem

The solutions displayed hereafter in the case of an skew-symmetric normal forcing are obtained exactly in the same way as those displayed before in the symmetric case. Let it be noted however that even if the structures are highly identical, the subfunctions appearing in the expressions of both $O(1)$ and $O(\eta)$ contributions are different and thus redefined in (B.6).

It is also very important to note that since the function W is different in the case of the skew-symmetric flapping compared to the symmetric case, so is the (p_m) sequence! A complete study of this one was made by Moffatt in [3].

B.1 $O(1)$ component of the stream function

In the case of an skew-symmetric normal and radial linear forcing, the order 0 component of the stream function can be expressed as follows

$$\hat{\psi}_0(r,\theta) = \begin{cases} -\sum_{m<0}\left(\frac{b^{p_m+2}-1}{r^{p_m}}\right)\left(\frac{f_m^1(\theta,\alpha)}{p_m}-\frac{f_m^2(\theta,\alpha)}{p_m+2}\right) & \text{if } r\leqslant 1 \\ \frac{r^2-1}{2}-\sum_{m<0}\frac{b^{p_m+2}}{r^{p_m}}\left(\frac{f_m^1(\theta,\alpha)}{p_m}-\frac{f_m^2(\theta,\alpha)}{p_m+2}\right)-\sum_{m>1}\frac{1}{r^{p_m}}\left(\frac{f_m^1(\theta,\alpha)}{p_m}-\frac{f_m^2(\theta,\alpha)}{p_m+2}\right) & \text{if } 1\leqslant r\leqslant b \\ \frac{b^2-1}{2}+\sum_{m>0}\left(\frac{b^{p_m+2}-1}{r^{p_m}}\right)\left(\frac{f_m^1(\theta,\alpha)}{p_m}-\frac{f_m^2(\theta,\alpha)}{p_m+2}\right) & \text{if } r\geqslant b \end{cases} \tag{B.1}$$

where

$$f_m^1(\theta,\alpha)=\frac{\sin[(p_m+2)\alpha]\cos(p_m\theta)}{\sin(2\alpha)+2\alpha\cos[2(p_m+1)\alpha]} \quad , \quad f_m^2(\theta,\alpha)=\frac{\sin(p_m\alpha)\cos[(p_m+2)\theta]}{\sin(2\alpha)+2\alpha\cos[2(p_m+1)\alpha]} \tag{B.2}$$

B.1.1 $O(\eta)$ component of the stream function

As it was the case for the $O(1)$ component, the $O(\eta)$ component of the stream function in the skew-symmetric flapping case shares high ressemblance in terms of structure with the one presented in the appendices (A.1), (A.2) and (A.3). However, the functions and coefficients interviening in its expression are slightly different as it can be observed below.

For $r\leqslant 1$, the solution takes the form

$$
\begin{aligned}
\hat{\psi}_1(r,\theta) =& 2i \sum_{m<0} \frac{(b^{p_m+4}-1)\left[p_m \sin(p_m\alpha)\cos[(p_m+2)\theta] - (p_m+2)\sin[(p_m+2)\alpha]\cos(p_m\theta)\right]}{W'(p_m)p_m^2(p_m+2)^2(p_m+4)r^{p_m}} \\
&+4i\sum_{n>0} X_n(b^{-p_n}-1)\frac{W(-p_n-4)\cos(p_n\theta) - \mathcal{U}_{p_n}(-p_n-4)\cos[(p_n+4)\theta] - \mathcal{V}_{p_n}(-p_n-4)\cos[(p_n+2)\theta}{32W(-p_n-4)(p_n+1)(p_n+2)r^{-p_n-4}} \\
&\quad - X_n(b^{-p_n+2}-1)\frac{\mathcal{U}'_{p_n}(-p_n-2)\cos[(p_n+2)\theta] + \left[\mathcal{V}'_{p_n}(-p_n-2) - W'(-p_n-2)\right]\cos(p_n\theta)]}{16W'(-p_n-2)(p_n+1)p_nW'(-p_n-2)r^{-p_n-2}} \\
&\quad + X_n \sum_{\substack{m<0\\ m\neq -n}} (b^{p_m+4}-1)\frac{\mathcal{U}_{p_m}(p_m)\cos(p_m\theta) + \mathcal{V}_{p_m}(p_m)\cos[(p_m+2)\theta]}{W'(p_m)(p_n+p_m+4)(p_n+p_m+2)(p_n-p_m+2)(p_n-p_m)(p_n+p_m)r^{p_m}} \\
&+4i\sum_{n>0} Y_n(b^{-p_n+2}-1)\frac{\mathcal{V}'_{p_n+2}(-p_n-2)\cos(p_n\theta) + \left[\mathcal{U}'_{p_n+2}(-p_n-2) - W'(-p_n-2)\right]\cos[(p_n+2)\theta]}{16W'(-p_n-2)(p_n+2)(p_n+1)p_nr^{-p_n-2}} \\
&\quad - Y_n \sum_{\substack{m<0\\ m\neq -n}} (b^{p_m+4}-1)\frac{\mathcal{U}_{p_m+2}(p_m)\cos(p_m\theta) + \mathcal{V}_{p_m+2}(p_m)\cos[(p_m+2)\theta]}{W'(p_m)(p_n+p_m+4)(p_n+p_m+2)(p_n-p_m+2)(p_n-p_m)(p_n+p_m)r^{p_m}}
\end{aligned}
\tag{B.3}
$$

Similarly, for $1 \leqslant r \leqslant b$, the solution is given by

$$
\begin{aligned}
\hat{\psi}_1(r,\theta) =& 2i \sum_{|m|>0} c_m^{p_m+4}\frac{\left[p_m \sin(p_m\alpha)\cos[(p_m+2)\theta] - (p_m+2)\sin[(p_m+2)\alpha]\cos(p_m\theta)\right]}{W'(p_m)p_m^2(p_m+2)^2(p_m+4)r^{p_m}} \\
&+4i\sum_{n>0} X_n b^{-p_n}\frac{W(-p_n-4)\cos(p_n\theta) - \mathcal{U}_{p_n}(-p_n-4)\cos[(p_n+4)\theta] - \mathcal{V}_{p_n}(-p_n-4)\cos[(p_n+2)\theta}{32W(-p_n-4)(p_n+1)(p_n+2)r^{-p_n-4}} \\
&\quad - X_n\frac{\mathcal{V}'_{p_n}(p_n)\cos[(p_n+2)\theta] + \left[\mathcal{U}'_{p_n}(p_n) - W'(p_n)\right]\cos(p_n\theta)}{16W'(p_n)p_n(p_n+1)(p_n+2)r^{p_n}} \\
&\quad - X_n b^{-p_n+2}\frac{\mathcal{U}'_{p_n}(-p_n-2)\cos[(p_n+2)\theta] + \left[\mathcal{V}'_{p_n}(-p_n-2) - W'(-p_n-2)\right]\cos(p_n\theta)]}{16W'(-p_n-2)(p_n+1)p_nW'(-p_n-2)r^{-p_n-2}} \\
&\quad + X_n \sum_{\substack{|m|>0\\ |m|\neq n}} c_m^{p_m+4}\frac{\mathcal{U}_{p_m}(p_m)\cos(p_m\theta) + \mathcal{V}_{p_m}(p_m)\cos[(p_m+2)\theta]}{W'(p_m)(p_n+p_m+4)(p_n+p_m+2)(p_n-p_m+2)(p_n-p_m)(p_n+p_m)r^{p_m}} \\
&+4i\sum_{n>0} Y_n b^{-p_n+2}\frac{\mathcal{V}'_{p_n+2}(-p_n-2)\cos(p_n\theta) + \left[\mathcal{U}'_{p_n+2}(-p_n-2) - W'(-p_n-2)\right]\cos[(p_n+2)\theta]}{16W'(-p_n-2)(p_n+2)(p_n+1)p_nr^{-p_n-2}} \\
&\quad + Y_n\frac{\mathcal{U}'_{p_n+2}(p_n)\cos(p_n\theta) + \left[\mathcal{V}'_{p_n+2}(p_n) - W'(p_n)\right]\cos[(p_n+2)\theta]}{16W'(p_n)p_n(p_n+1)(p_n+2)r^{p_n}} \\
&\quad + Y_n\frac{W(p_n-2)\cos[(p_n+2)\theta] - \mathcal{U}'_{p_n+2}(p_n-2)\cos[(p_n-2)\theta] - \mathcal{V}'_{p_n+2}(p_n-2)\cos(p_n\theta)}{32W(p_n-2)p_n(p_n+1)r^{p_n-2}} \\
&\quad - Y_n \sum_{\substack{|m|>0\\ |m|\neq n}} c_m^{p_m+4}\frac{\mathcal{U}_{p_m+2}(p_m)\cos(p_m\theta) + \mathcal{V}_{p_m+2}(p_m)\cos[(p_m+2)\theta]}{W'(p_m)(p_n+p_m+4)(p_n+p_m+2)(p_n-p_m+2)(p_n-p_m)(p_n+p_m)r^{p_m}} \\
&+ \frac{ir^4}{32W(-4)}\left[W(-4) + 4\sin(4\alpha\cos(2\theta) - 2\sin(2\alpha)\cos(4\theta)\right]
\end{aligned}
\tag{B.4}
$$

And finally for $r \geqslant b$

$$
\begin{aligned}
\hat{\psi}_1(r,\theta) = &-2i\sum_{m>0}(b^{p_m+4}-1)\frac{\left[p_m\sin(p_m\alpha)\cos[(p_m+2)\theta]-(p_m+2)\sin[(p_m+2)\alpha]\cos(p_m\theta)\right]}{W'(p_m)p_m^2(p_m+2)^2(p_m+4)r^{p_m}}\\
&+4i\sum_{n>0}X_n(b^{p_n+4}-1)\frac{\mathcal{V}'_{p_n}(p_n)\cos[(p_n+2)\theta]+\left[\mathcal{U}'_{p_n}(p_n)-W'(p_n)\right]\cos(p_n\theta)}{16W'(p_n)p_n(p_n+1)(p_n+2)r^{p_n}}\\
&-X_n\sum_{\substack{m>0\\m\neq n}}(b^{p_m+4}-1)\frac{\mathcal{U}_{p_m}(p_m)\cos(p_m\theta)+\mathcal{V}_{p_m}(p_m)\cos[(p_m+2)\theta]}{W'(p_m)(p_n+p_m+4)(p_n+p_m+2)(p_n-p_m+2)(p_n-p_m)(p_n+p_m)r^{p_m}}\\
&-4i\sum_{n>0}Y_n(b^{p_n+4}-1)\frac{\mathcal{U}'_{p_n+2}(p_n)\cos(p_n\theta)+\left[\mathcal{V}'_{p_n+2}(p_n)-W'(p_n)\right]\cos[(p_n+2)\theta]}{16W'(p_n)p_n(p_n+1)(p_n+2)r^{p_n}}\\
&+Y_n(b^{p_n+2}-1)\frac{W(p_n-2)\cos[(p_n+2)\theta]-\mathcal{U}'_{p_n+2}(p_n-2)\cos[(p_n-2)\theta]-\mathcal{V}'_{p_n+2}(p_n-2)\cos(p_n\theta)}{32W(p_n-2)p_n(p_n+1)r^{p_n-2}}\\
&-Y_n\sum_{\substack{m>0\\m\neq n}}(b^{p_m+4}-1)\frac{\mathcal{U}_{p_m+2}(p_m)\cos(p_m\theta)+\mathcal{V}_{p_m+2}(p_m)\cos[(p_m+2)\theta]}{W'(p_m)(p_n+p_m+4)(p_n+p_m+2)(p_n-p_m+2)(p_n-p_m)(p_n+p_m)r^{p_m}}
\end{aligned}
\tag{B.5}
$$

where c_m is defined in the same way as in (A.3) and

$$
\begin{cases}
\mathcal{U}_\xi(p)=(p+2)\sin[(p+2)\alpha]\cos(\xi\alpha)-\xi\sin(\xi\alpha)\cos[(p+2)\alpha]\\
\mathcal{V}_\xi(p)=\xi\sin(\xi\alpha)\cos(p\alpha)-p\sin(p\alpha)\cos(\xi\alpha)\\
W(p)=(p+1)\sin(2\alpha)+\sin[2(p+1)\alpha]
\end{cases}
,\quad
\begin{cases}
X_m=\dfrac{(p_m+1)\sin[(p_m+2)\alpha]}{p_m\left(\sin(2\alpha)+2\alpha\cos[2(p_m+1)\alpha]\right)}\\
Y_m=\dfrac{(p_m+1)\sin(p_m\alpha)}{(p_m+2)\left(\sin(2\alpha)+2\alpha\cos[2(p_m+1)\alpha]\right)}
\end{cases}
\tag{B.6}
$$

Appendix C

Full solution to a tangential and skew-symmetric boundary forcing problem

The exact solution for an skew-symmetric tangential boundary forcing was determined by my Mr.Branicki in the same fashion as the ones exposed before. Since the symmetry is the same as in (B), the W function is the same and the sub functions interviening in the expression of $\hat{\psi}_1$ are going to be the same.

C.1 $O(1)$ component of the stream function

In the same fashion as before, the leading part of the stream function $\hat{\psi}_0$ takes the following form

$$\hat{\psi}_0(r,\theta) = \begin{cases} \displaystyle\sum_{n<0} \frac{b^{p_n+1}-1}{p_n+1}\frac{f_n(\theta,\alpha)}{r^{p_n}}, & r \leqslant 1, \\ \displaystyle\sum_{n<0} \frac{b^{p_n+1}}{p_n+1}\frac{f_n(\theta,\alpha)}{r^{p_n}} + \sum_{n>0} \frac{1}{p_n+1}\frac{f_n(\theta,\alpha)}{r^{p_n}} + 2rg(\theta,\alpha), & 1 \leqslant r \leqslant b, \\ \displaystyle -\sum_{n>0} \frac{b^{p_n+1}-1}{p_n+1}\frac{f_n(\theta,\alpha)}{r^{p_n}}, & r \geqslant b, \end{cases} \tag{C.1}$$

where

$$f_n(\theta,\alpha) = \frac{\cos(p_n\theta)\cos[(p_n+2)\alpha] - \cos(p_n\alpha)\cos[(p_n+2)\theta]}{\sin(2\alpha)+2\alpha\cos[2(p_n+1)\alpha]} \quad , \quad g(\theta,\alpha) = \frac{\cos(\alpha)\theta\sin(\theta) - \alpha\sin(\alpha)\cos(\theta)}{\sin(2\alpha)+2\alpha} \tag{C.2}$$

C.2 $O(\eta)$ component of the stream function

Again, in the same way as in (B), the $O(\eta)$ term can be calculated using the same method as in (I.1). The expression is highly similar to the one corresponding to $\hat{\psi}_1$ in the appendix (B).

For $r \leqslant 1$, $\hat{\psi}_1$ is given by

$$
\begin{aligned}
\hat{\psi}_1(r,\theta) =& 4iZ \sum_{m>0} \frac{(b^{-p_m+3}-1)\left[\mathcal{U}_1(-p_m-2)\cos[(p_m+2)\theta]+\mathcal{V}_1(-p_m-2)\cos(p_m\theta)\right]}{W'(p_m)(p_m-1)^2(p_m+1)^2(p_m+3)r^{-p_m-2}} \\
&+4i\sum_{n>0} X_n(b^{-p_n}-1)\frac{W(-p_n-4)\cos(p_n\theta)-\mathcal{U}_{p_n}(-p_n-4)\cos[(p_n+4)\theta]-\mathcal{V}_{p_n}(-p_n-4)\cos[(p_n+2)\theta}{32W(-p_n-4)(p_n+1)(p_n+2)r^{-p_n-4}} \\
&\quad -X_n(b^{-p_n+1}-1)\frac{\mathcal{U}'_{p_n}(-p_n-2)\cos[(p_n+2)\theta]+\left[\mathcal{V}'_{p_n}(-p_n-2)-W'(-p_n-2)\right]\cos(p_n\theta)]}{16W'(-p_n-2)(p_n+1)p_nW'(-p_n-2)r^{-p_n-2}} \\
&\quad +X_n\sum_{\substack{m<0\\ m\neq -n}}(b^{p_m+3}-1)\frac{\mathcal{U}_{p_m}(p_m)\cos(p_m\theta)+\mathcal{V}_{p_m}(p_m)\cos[(p_m+2)\theta]}{W'(p_m)(p_n+p_m+4)(p_n+p_m+2)(p_n-p_m+2)(p_n-p_m)(p_n+p_m)r^{p_m}} \\
&+4i\sum_{n>0} Y_n(b^{-p_n+1}-1)\frac{\mathcal{V}'_{p_n+2}(-p_n-2)\cos(p_n\theta)+\left[\mathcal{U}'_{p_n+2}(-p_n-2)-W'(-p_n-2)\right]\cos[(p_n+2)\theta]}{16W'(-p_n-2)(p_n+2)(p_n+1)p_nr^{-p_n-2}} \\
&\quad -Y_n\sum_{\substack{m<0\\ m\neq -n}}(b^{p_m+4}-1)\frac{\mathcal{U}_{p_m+2}(p_m)\cos(p_m\theta)+\mathcal{V}_{p_m+2}(p_m)\cos[(p_m+2)\theta]}{W'(p_m)(p_n+p_m+4)(p_n+p_m+2)(p_n-p_m+2)(p_n-p_m)(p_n+p_m)r^{p_m}}
\end{aligned}
\tag{C.3}
$$

Similarly, for $1 \leqslant r \leqslant b$

$$
\begin{aligned}
\hat{\psi}_1(r,\theta) =& 4iZ \sum_{|m|>0} c_m^{p_m+3}\frac{\left[\mathcal{U}_1(p_m)\cos(p_m\theta)+\mathcal{V}_1(p_m)\cos[(p_m+2)\theta]\right]}{W'(p_m)(p_m-1)(p_m+1)^2(p_m+3)^2r^{-p_m-2}} \\
&+4i\sum_{n>0} X_n b^{-p_n-1}\frac{W(-p_n-4)\cos(p_n\theta)-\mathcal{U}_{p_n}(-p_n-4)\cos[(p_n+4)\theta]-\mathcal{V}_{p_n}(-p_n-4)\cos[(p_n+2)\theta}{32W(-p_n-4)(p_n+1)(p_n+2)r^{-p_n-4}} \\
&\quad -X_n\frac{\mathcal{V}'_{p_n}(p_n)\cos[(p_n+2)\theta]+\left[\mathcal{U}'_{p_n}(p_n)-W'(p_n)\right]\cos(p_n\theta)}{16W'(p_n)p_n(p_n+1)(p_n+2)r^{p_n}} \\
&\quad -X_n b^{-p_n+1}\frac{\mathcal{U}'_{p_n}(-p_n-2)\cos[(p_n+2)\theta]+\left[\mathcal{V}'_{p_n}(-p_n-2)-W'(-p_n-2)\right]\cos(p_n\theta)]}{16W'(-p_n-2)(p_n+1)p_nW'(-p_n-2)r^{-p_n-2}} \\
&\quad +X_n\sum_{\substack{|m|>0\\ |m|\neq n}} c_m^{p_m+4}\frac{\mathcal{U}_{p_m}(p_m)\cos(p_m\theta)+\mathcal{V}_{p_m}(p_m)\cos[(p_m+2)\theta]}{W'(p_m)(p_n+p_m+4)(p_n+p_m+2)(p_n-p_m+2)(p_n-p_m)(p_n+p_m)r^{p_m}} \\
&+4i\sum_{n>0} Y_n b^{-p_n+1}\frac{\mathcal{V}'_{p_n+2}(-p_n-2)\cos(p_n\theta)+\left[\mathcal{U}'_{p_n+2}(-p_n-2)-W'(-p_n-2)\right]\cos[(p_n+2)\theta]}{16W'(-p_n-2)(p_n+2)(p_n+1)p_nr^{-p_n-2}} \\
&\quad +Y_n\frac{\mathcal{U}'_{p_n+2}(p_n)\cos(p_n\theta)+\left[\mathcal{V}'_{p_n+2}(p_n)-W'(p_n)\right]\cos[(p_n+2)\theta]}{16W'(p_n)p_n(p_n+1)(p_n+2)r^{p_n}} \\
&\quad +Y_n\frac{W(p_n-2)\cos[(p_n+2)\theta]-\mathcal{U}'_{p_n+2}(p_n-2)\cos[(p_n-2)\theta]-\mathcal{V}'_{p_n+2}(p_n-2)\cos(p_n\theta)}{32W(p_n-2)p_n(p_n+1)r^{p_n-2}} \\
&\quad -Y_n\sum_{\substack{|m|>0\\ |m|\neq n}} c_m^{p_m+4}\frac{\mathcal{U}_{p_m+2}(p_m)\cos(p_m\theta)+\mathcal{V}_{p_m+2}(p_m)\cos[(p_m+2)\theta]}{W'(p_m)(p_n+p_m+4)(p_n+p_m+2)(p_n-p_m+2)(p_n-p_m)(p_n+p_m)r^{p_m}} \\
&+\frac{r^3}{32}\left[\frac{(3-4\cos^2\alpha)\sin 2\alpha-2\alpha(4\cos 2\alpha\sin^2\alpha+1)}{(\sin 2\alpha+2\alpha)\sin 2\alpha\cos\alpha}\cos\theta+\frac{8\cos\alpha}{\sin 2\alpha+2\alpha}\theta\sin\theta+\frac{\cos 3\theta}{\sin 2\alpha\cos\alpha}\right]
\end{aligned}
\tag{C.4}
$$

And finally, for $r \geqslant b$

$$
\begin{aligned}
\hat{\psi}_1(r,\theta) =& 4iZ \sum_{m>0} (b^{p_m+3}-1) \frac{\left[\mathcal{U}_1(p_m)\cos(p_m\theta) + \mathcal{V}_1(p_m)\cos[(p_m+2)\theta]\right]}{W'(p_m)p_m^2(p_m+2)^2(p_m+4)r^{p_m}} \\
&+ 4i \sum_{n>0} X_n (b^{p_n+3}-1) \frac{\mathcal{V}'_{p_n}(p_n)\cos[(p_n+2)\theta] + \left[\mathcal{U}'_{p_n}(p_n) - W'(p_n)\right]\cos(p_n\theta)}{16W'(p_n)p_n(p_n+1)(p_n+2)r^{p_n}} \\
&- X_n \sum_{\substack{m>0 \\ m\neq n}} (b^{p_m+3}-1) \frac{\mathcal{U}_{p_m}(p_m)\cos(p_m\theta) + \mathcal{V}_{p_m}(p_m)\cos[(p_m+2)\theta]}{W'(p_m)(p_n+p_m+4)(p_n+p_m+2)(p_n-p_m+2)(p_n-p_m)(p_n+p_m)r^{p_m}} \\
&- 4i \sum_{n>0} Y_n (b^{p_n+3}-1) \frac{\mathcal{U}'_{p_n+2}(p_n)\cos(p_n\theta) + \left[\mathcal{V}'_{p_n+2}(p_n) - W'(p_n)\right]\cos[(p_n+2)\theta]}{16W'(p_n)p_n(p_n+1)(p_n+2)r^{p_n}} \\
&+ Y_n (b^{p_n+1}-1) \frac{W(p_n-2)\cos[(p_n+2)\theta] - \mathcal{U}'_{p_n+2}(p_n-2)\cos[(p_n-2)\theta] - \mathcal{V}'_{p_n+2}(p_n-2)\cos(p_n\theta)}{32W(p_n-2)p_n(p_n+1)r^{p_n-2}} \\
&- Y_n \sum_{\substack{m>0 \\ m\neq n}} (b^{p_m+3}-1) \frac{\mathcal{U}_{p_m+2}(p_m)\cos(p_m\theta) + \mathcal{V}_{p_m+2}(p_m)\cos[(p_m+2)\theta]}{W'(p_m)(p_n+p_m+4)(p_n+p_m+2)(p_n-p_m+2)(p_n-p_m)(p_n+p_m)r^{p_m}}
\end{aligned}
\tag{C.5}
$$

Where the functions $\mathcal{U}_\bullet(\bullet)$, $\mathcal{V}_\bullet(\bullet)$ and W are given by (B.6) and the coefficients X_n, Y_n and Z by :

$$
X_n = \frac{\cos[(p_n+2)\alpha]}{\sin 2\alpha + 2\alpha\cos[2(p_n+1)\alpha]} \quad , \quad Y_n = \frac{\cos(p_n\alpha)}{\sin(2\alpha) + 2\alpha\cos[2(p_n+1)\alpha]} \quad , \quad Z = \frac{\cos(\alpha)}{\sin(2\alpha)+2\alpha} \tag{C.6}
$$

Appendix D

Symmetric normal boundary forcing : properties of series expansions

In order to know whether the truncated series used in our numerical computations yield a satisfying approximation for $\hat{\psi}_0$ and $\hat{\psi}_1$ and the velocity fields they induce, it is important to determine at what rate those series converge.

Be it in one of the flapping cases or in the that of the tangential oscillation, the proofs and convergence studies that follow will be similar in nature. Thus, we restricted ourselves here to the case of the symmetric normal boundary flapping.

D.1 Convergence of the series expansion in $\hat{\psi}_0$

We are now going to study the convergence of the series expansions describing the function $\hat{\psi}_0$ with respect to the L^2 norm on the domain $]0,+\infty[\times[-\alpha,\alpha]$ which we shall note $\|\bullet\|_{L^2}$. In order to do so, let us define the function representing $\hat{\psi}_0$ truncated at rank N and call it $\hat{\psi}_0^N$. In the following development, we show that :

$$\| \hat{\psi}_0 - \hat{\psi}_0^N \|_{L^2} \leqslant R_N \underset{+\infty}{\sim} 4\alpha\sqrt{\frac{2\ln(2)(b^6+b^2+5)}{\pi^3 N}} \tag{D.1}$$

This quantity can be expressed as follows :

$$\begin{aligned}\| \hat{\psi}_0 - \hat{\psi}_0^N \|_{L^2}^2 &= \int_0^{+\infty}\int_{-\alpha}^{\alpha} |\hat{\psi}_0(r,\theta) - \hat{\psi}_0^N(r,\theta)|^2 r\,\mathrm{d}r\,\mathrm{d}\theta \\ &= \int_0^{1}\int_{-\alpha}^{\alpha} |\hat{\psi}_0(r,\theta) - \hat{\psi}_0^N(r,\theta)|^2 r\,\mathrm{d}r\,\mathrm{d}\theta + \int_1^{b}\int_{-\alpha}^{\alpha} |\hat{\psi}_0(r,\theta) - \hat{\psi}_0^N(r,\theta)|^2 r\,\mathrm{d}r\,\mathrm{d}\theta + \int_b^{+\infty}\int_{-\alpha}^{\alpha} |\hat{\psi}_0(r,\theta) - \hat{\psi}_0^N(r,\theta)|^2 r\,\mathrm{d}r\,\mathrm{d}\theta\end{aligned} \tag{D.2}$$

We are now going to estimate and majorate each of those integrales. But first of all, let us focus a bit on the equivalents $(p_m)_{m>1}$ could yield for m going to infinity.

D.1.1 Quick study of the $(p_m)_{m>1}$ sequence for m going to infinity

Let us define ξ_m and η_m such that $p_m = \xi_m + i\eta_m$. We already know that

$$\frac{\pi}{\alpha}\left\lfloor\frac{m}{2}\right\rfloor \leqslant \xi_m + 1 \leqslant \frac{\pi}{\alpha}\left(\left\lfloor\frac{m}{2}\right\rfloor + \frac{1}{2}\right) \quad\Longrightarrow\quad \xi_m \underset{+\infty}{\sim} \frac{\pi}{\alpha}\left\lfloor\frac{m}{2}\right\rfloor \tag{D.3}$$

Moreover, we know by definition that $W(p_m) = 0$, which, upon taking the square modulus of the expresion leads to :

$$\sin^2(2\alpha)\left[(\xi_m+2)^2+\eta_m^2\right] = \cos^2[2(\xi_m+1)\alpha]\mathrm{ch}^2(2\alpha\eta_m) + \sin^2[2(\xi_m+1)\alpha]\mathrm{sh}^2(2\alpha\eta_m)$$

From which it is possible to extract the following equivalent for η_m

$$\mathrm{e}^{4\alpha\eta_m} \underset{+\infty}{\sim} 2\sin^2(2\alpha)\left(\frac{\pi}{\alpha}\left\lfloor\frac{m}{2}\right\rfloor\right)^2 \tag{D.4}$$

Plus, let us not forget that evidently, $\left\lfloor\frac{m}{2}\right\rfloor \underset{+\infty}{\sim} \frac{m}{2}$

D.1.2 Majoration of the L^2 norm : detailed for the case $r \in [0,1[$

Let us define for all $m \in \mathbb{Z}\setminus\{-1,0,1\}$, $p_m = \xi_m + i\eta_m$. For $r<1$, the expression of $\hat{\psi}_0$ given by (I.21) yields :

$$\begin{aligned}\left|\hat{\psi}_0(r,\theta)-\hat{\psi}_0^N(r,\theta)\right| &= \left|\sum_{m<-N}\left(\frac{b^{p_m+2}-1}{r^{p_m}}\right)\left(\frac{f_m^1(\theta,\alpha)}{p_m}-\frac{f_m^2(\theta,\alpha)}{p_m+2}\right)\right| \\ &= \left|\sum_{m>N}\left(b^{-p_m}-1\right)r^{p_m+2}\left(\frac{f_m^1(\theta,\alpha)}{p_m}-\frac{f_m^2(\theta,\alpha)}{p_m+2}\right)\right| \\ &\leqslant \sum_{m>N}\left|b^{-p_m}-1\right|r^{\xi_m+2}\left(\frac{\left|f_m^1(\theta,\alpha)\right|+\left|f_m^2(\theta,\alpha)\right|}{|p_m+2|}\right)\end{aligned} \tag{D.5}$$

Moreover, it is possible to establish the following bounds for $f_m^1(\theta,\alpha)$ and $f_m^2(\theta,\alpha)$:

$$\forall m\in\mathbb{Z}\setminus\{-1,0,1\}\ ,\ \forall\theta\in[-\alpha,\alpha]\ ,\ \begin{cases}\left|f_m^1(\theta,\alpha)\right| \leqslant \dfrac{\mathrm{ch}^2(\alpha\eta_m)}{\sqrt{4\alpha^2\mathrm{sh}^2(2\alpha\eta_m)-4\alpha\sin(2\alpha)\mathrm{ch}(2\alpha\eta_m)}} \\ \left|f_m^2(\theta,\alpha)\right| \leqslant \dfrac{\mathrm{ch}^2(\alpha\eta_m)}{\sqrt{4\alpha^2\mathrm{sh}^2(2\alpha\eta_m)-4\alpha\sin(2\alpha)\mathrm{ch}(2\alpha\eta_m)}}\end{cases} \tag{D.6}$$

We can then conclude remarking that $b^{-\xi_m} \leqslant 1 \quad \forall m>1$ that

$$\left|\hat{\psi}_0(r,\theta)-\hat{\psi}_0^N(r,\theta)\right| \leqslant 4\sum_{m>N}\frac{r^{\xi_m+2}\mathrm{ch}^2(\alpha\eta_m)}{|p_m+2|\sqrt{4\alpha^2\mathrm{sh}^2(2\alpha\eta_m)-4\alpha\sin(2\alpha)\mathrm{ch}(2\alpha\eta_m)}} = 4\sum_{m>N}A_m(r,\alpha) \tag{D.7}$$

and thus that

$$\begin{aligned}&\left|\hat{\psi}_0(r,\theta)-\hat{\psi}_0^N(r,\theta)\right|^2 \leqslant 16\sum_{m,n>N}A_m(r,\alpha)A_n(r,\alpha) \\ \Longrightarrow\quad &\int_0^1\int_{-\alpha}^{\alpha}|\hat{\psi}_0(r,\theta)-\hat{\psi}_0^N(r,\theta)|^2 r\,\mathrm{d}r\,\mathrm{d}\theta \leqslant 32\alpha\sum_{m,n>N}\int_0^1 A_m(r,\alpha)A_n(r,\alpha)r\,\mathrm{d}r\end{aligned} \tag{D.8}$$

upon invoking the dominated convergence theorem of Lebesgue.

We can then proceed to calculate these integrals and give an equivalent for N going to infinity for them. The calculation first yields

$$\int_0^1 A_m(r,\alpha)A_n(r,\alpha)r\,\mathrm{d}r = \frac{\frac{1}{\sqrt{((\xi_m+2)^2+\eta_m^2)((\xi_n+2)^2+\eta_n^2)}}\mathrm{ch}^2(\alpha\eta_m)\mathrm{ch}^2(\alpha\eta_n)}{(\xi_m+\xi_n+6)\sqrt{\left[4\alpha^2\mathrm{sh}^2(2\alpha\eta_m)-4\alpha\sin(2\alpha)\mathrm{ch}(2\alpha\eta_m)\right]\left[4\alpha^2\mathrm{sh}^2(2\alpha\eta_n)-4\alpha\sin(2\alpha)\mathrm{ch}(2\alpha\eta_n)\right]}} \tag{D.9}$$

Using the equivalents described in (D.3) and (D.4) for $(\xi_m)_{m>1}$ and $(\eta_m)_{m>1}$, we can give the following for the integral (D.9).

$$\int_0^1 A_m(r,\alpha)A_n(r,\alpha)r\,\mathrm{d}r \underset{+\infty}{\sim} \frac{2\alpha}{\pi^3 mn(m+n)} \tag{D.10}$$

Consequent to remarking that both functions $x \longrightarrow \frac{1}{xy(x+y)}$, $y>N$ and $y \longrightarrow \frac{1}{xy(x+y)}$, $x>N$ decrease on $[N+1,+\infty[$, it is possible to give the following equivalent of the double series using an integrale framing

$$\sum_{m,n>N}\frac{1}{mn(m+n)} \underset{+\infty}{\sim} \frac{2\ln(2)}{N} \tag{D.11}$$

Thus, finally

$$\sum_{m,n>N} \int_0^1 A_m(r,\alpha)A_n(r,\alpha)r\mathrm{d}r \underset{+\infty}{\sim} \frac{4\ln(2)\alpha}{\pi^3 N} \tag{D.12}$$

Which yields after defining the total majorant M_N^1 for conveniency

$$\int_0^1 \int_{-\alpha}^{\alpha} |\hat{\psi}_0(r,\theta) - \hat{\psi}_0^N(r,\theta)|^2 r\mathrm{d}r\mathrm{d}\theta \leqslant M_N^1 \underset{+\infty}{\sim} \frac{128\ln(2)\alpha^2}{\pi^3 N} \tag{D.13}$$

D.1.3 Total majoration of the remainder of the series expansion

Similarly, it can be shown that

$$\begin{cases} A_m(r,\theta) = \dfrac{\left(b^{-\xi_m} r^{\xi_m+2} + r^{-\xi_m}\right)\mathrm{ch}^2(\alpha\eta_m)}{2|p_m+2|\sqrt{4\alpha^2\mathrm{sh}^2(2\alpha\eta_m) - 4\alpha\sin(2\alpha)\mathrm{ch}(2\alpha\eta_m)}} & \text{if } 1 \leqslant r \leqslant b \\ A_m(r,\theta) = \dfrac{r^{-\xi_m}\left(b^{\xi_m+2}+1\right)\mathrm{ch}^2(\alpha\eta_m)}{2|p_m+2|\sqrt{4\alpha^2\mathrm{sh}^2(2\alpha\eta_m) - 4\alpha\sin(2\alpha)\mathrm{ch}(2\alpha\eta_m)}} & \text{if } b \leqslant r \end{cases} \tag{D.14}$$

which leads to the following equivalents

$$\int_1^b A_m(r,\alpha)A_n(r,\alpha)r\mathrm{d}r \underset{+\infty}{\sim} \frac{(1+b^6)\alpha}{\pi^3 mn(m+n)} \quad , \quad \int_b^{+\infty} A_m(r,\alpha)A_n(r,\alpha)r\mathrm{d}r \underset{+\infty}{\sim} \frac{b^2\alpha}{\pi^3 mn(m+n)} \tag{D.15}$$

We finally have the following majoration of the L^2 remainder for $\hat{\psi}_0^N$

$$\| \hat{\psi}_0 - \hat{\psi}_0^N \|_{L^2} \leqslant R_N \underset{+\infty}{\sim} 4\alpha\sqrt{\frac{2\ln(2)(b^6+b^2+5)}{\pi^3 N}} \tag{D.16}$$

We can see here that the convergence with respect to the L^2 norm is rather slow for the stream function. Since the action of differentiating $\hat{\psi}_0$ with respect to r or θ will have the effect of multiplying it by a linear function of p_m thereby slowering its convergence, we can then have the insight that the velocity series expansions are not expected to converge with respect to the L^2 norm.

D.2 Concerning the series expansions in $\hat{\psi}_1$

As it can be foreseen easily by having a look at the appendices (A.1), (A.2) and (A.3), performing the same convergence analysis as we did for $\hat{\psi}_0$ on $\hat{\psi}_1$ would be likely to entail intractable differentiation. However, some qualitative remarks can be made on that subject.

Indeed, it is possible to see that the nature of the trigonometric functions appearing in $\hat{\psi}_1$ is roughly the same as those in $\hat{\psi}_0$, meaning that they should yield convergence properties of the same kind based on their high symetries.

Yet in this case, these trigonometric functions are multiplied by p_m^{-5} and not p_m^{-1}, meaning that the convergence should be faster for the order 1 stream function's truncated series.

This reasonable assumption can be verified empirically by plotting $\hat{\psi}_1$ and the velocity field derived from it and seeing that the results look smoother for small numbers of terms (compare figures II.7 to II.8 for instance). Besides, they do not suffer from the same high sensitivity with respect to numerical errors on the p_ms' values as the order 0 velocities (see appendix D.4).

D.3 Pointwise convergence of the order 0 velocity series expansions at the interfaces $r = 1$ and $r = b$

We are now going to study the convergence of the series expansions used in the expressions of the velocity components derived from $\hat{\psi}_0$ at the different interfaces of the domain.

Recall that, in polar coordinates, the velocity field (v_r, v_θ) associated to a given stream function ψ is given by

$$v_r(r,\theta) = \frac{1}{r}\frac{\partial \psi}{\partial \theta}(r,\theta) \quad , \quad v_\theta(r,\theta) = -\frac{\partial \psi}{\partial r}(r,\theta) \tag{D.17}$$

After a quick glance at the convergence of thoses series expansions, we came to the realization that we were not going to obtain any kind of uniform convergence as it was the case for $\hat{\psi}_0$ in L^2-norm . The pointwise convergence remains however strong due to the exponentially-decreasing terms in r present in each series expansions. But those terms tend to weight very little upon taking r close to 1 or b. It is then necessary to study precisely the convergence of the series expansions along those interfaces.

D.3.1 Expression of the series expansions' errors on the interface

Let us start this convergence study by a small remark :

> It has been noted in section I.2.3 that the function $p \longmapsto \left|p^2 \hat{\Psi}_0(p,\theta)\right|$ was bounded regardless of θ within the maximal holomorphy strip defined in (I.23).

Moreover, using the properties of the Mellin transform detailed in I.14 and I.15 ,it can be shown that the velocity components $v_{r,0}$ and $v_{\theta,0}$ derived from $\hat{\psi}_0$ do verify

$$\begin{cases} \mathcal{M}[v_{r,0}](p) = \mathcal{M}\left[\dfrac{1}{r}\dfrac{\partial \hat{\psi}_0}{\partial \theta}\right](p) = \dfrac{\mathrm{d}}{\mathrm{d}\theta}\left[\mathcal{M}\left[\hat{\psi}_0\right](p-1)\right] \\ \mathcal{M}[v_{\theta,0}](p) = \mathcal{M}\left[-\dfrac{\partial \hat{\psi}_0}{\partial r}\right](p) = (p-1)\mathcal{M}\left[\hat{\psi}_0\right](p-1) \end{cases} \tag{D.18}$$

It is possible to show that these two complex variable functions are majorized by $p \longmapsto K|p-1|^{-2}$ within $S(\hat{\psi}_0,\delta) \cap \left]\mathcal{R}[p_{-2}]+1, \mathcal{R}[p_2]+1\right[$ where $K > 0$. Thus, the two components of velocity v_r^0 and v_θ^0 given by the inverse transforms of the previously described functions are continuous.

Hence, let us define now the truncated functions $v_{r,0}$ and $v_{\theta,0}$ in the form

$$\begin{cases} v_{r,0}^N(r,\theta) = v_{r,0}(r,\theta) - \delta v_{r,0}^N(r,\theta) \\ v_{\theta,0}^N(r,\theta) = v_{\theta,0}(r,\theta) - \delta v_{\theta,0}^N(r,\theta) \end{cases} \quad \text{where } \delta v_{\theta,0}^N \text{ and } \delta v_{r,0}^N \text{ are truncation errors} \tag{D.19}$$

Since both velocity components are continuous, it is possible to define the truncation errors at the interfaces as

$$\begin{cases} \delta_{r,1}^N = \delta v_{r,0}^N(1^+,\theta) - \delta v_{r,0}^N(1^-,\theta) \text{ and } \delta_{\theta,1}^N = \delta v_{\theta,0}^N(1^+,\theta) - \delta v_{\theta,0}^N(1^-,\theta) \text{ at the interface } r = 1 \\ \delta_{r,b}^N = \delta v_{r,0}^N(b^+,\theta) - \delta v_{r,0}^N(b^-,\theta) \text{ and } \delta_{\theta,b}^N = \delta v_{\theta,0}^N(b^+,\theta) - \delta v_{\theta,0}^N(b^-,\theta) \text{ at the interface } r = b \end{cases} \tag{D.20}$$

From the analytical expression of $\hat{\psi}_0$ and from (II.1), it is possible to see that

$$\delta_{r,1}^N = \delta_{r,b}^N = 0 \quad \forall N > 0 \tag{D.21a}$$

$$\delta_{\theta,1}^N = \delta_{\theta,b}^N = 2\sum_{m>N}(p_m+1)\left(\frac{f_m^1(\theta,\alpha)}{p_m} - \frac{f_m^2(\theta,\alpha)}{p_m+2}\right) \quad \forall N > 0 \tag{D.21b}$$

The result given (D.21a) is consistent with what can be observerd when plotting the radial component of velocity field, id est that the radial velocity is continuous for any given N at the interfaces.

Let us now refine the form of the expression given by (D.21b) in order to study the convergence of the error made on the angular velocity.

D.3.2 Analysis of the convergence of the truncating error made on the angular velocity at the interfaces

It is not possible to majorize the angular velocity errors in (D.21b) by simply using a modulus majoration since the series remainders converge only because of the oscillating properties of their general terms. These can nevertheless be estimated as follows.

It is clear that $\xi_m + k \underset{+\infty}{\sim} \xi_m$ for any fixed k. We can then write that $p_m + 1 \underset{+\infty}{\sim} p_m$ and $p_m + 2 \underset{+\infty}{\sim} p_m$ in the sense that both their real and imaginary part are equivalents as sequences of real numbers.

In that sens, it is possible to write that $(p_m+1)\left(\frac{f_m^1(\theta,\alpha)}{p_m} - \frac{f_m^2(\theta,\alpha)}{p_m+2}\right) \underset{+\infty}{\sim} f_m^1(\theta,\alpha) - f_m^2(\theta,\alpha)$.

After quite some algebra and by using the equivalents given by (D.3) and (D.4), it is possible to show that :

$$f_m^1(\theta,\alpha) - f_m^2(\theta,\alpha) \underset{+\infty}{\sim} -\frac{\sin\left[\left(\left\lfloor\frac{m}{2}\right\rfloor\frac{\pi}{\alpha}+2\right)(\alpha-\theta)\right] - \sin\left[\left\lfloor\frac{m}{2}\right\rfloor\frac{\pi}{\alpha}(\alpha-\theta)\right]}{\left(\frac{\sin(2\alpha)\pi}{\alpha\sqrt{2}}m\right)^{\frac{1}{2}\left(1-\frac{\theta}{\alpha}\right)}} \tag{D.22}$$

The numerator is a function increasingly oscillating as m grows at any given θ and that tends sufficiently fast toward zero when $\theta \longrightarrow \alpha$ so that the series expansion is still convergent near $\theta = \alpha$.

This result is also consistent with what can be observed, namely that at the interface, the angular velocity is oscillating from either side in an opposite phases-pattern which period seems to grow linearly with N.

However, the convergence is theoretically very weak, and as mentioned before, the amplitude of the oscillations do not numerically converge toward zero for both of the velocity fields. This most odd behaviour can luckily be explained and does not invalidate our previous convergence results, and that is what we do in the coming section.

D.4 Sensitivity of the series expansions with respect to small errors on the numerical values of the $(p_m)_{m>1}$ sequence

After plotting the velocity fields derived from $\hat{\psi}_0$ for growing numbers of p_ms, an alarming assessment had to be made : the amplitude of the peaks in both the radial and angular velocities did not seem to decrease as they should have. More intriguing still, this problem seemed only to concern the velocities derived from $\hat{\psi}_0$.

At this point, let us remind ourselves that the stream function was demonstrated to be $\mathcal{C}^4$. So even with a slow convergence rate, velocities are supposed to converge toward something smooth and at the very least $\mathcal{C}^1$. So why is it not actually the case?

This can be explained by looking at the effect an error ϵ occuring while numerically evaluating the p_ms can have. Let it be noted that since the resulting expressions' size were absurdly large, these calculations have been carried out using Maple.

Taking the Taylor expansion of the different series general terms with respect to ϵ yields in each case a term of the form $O(R(p_m)\epsilon)$ were R is a function depending on the series expansion considered.

A quick study of $p \longmapsto R(p)$ in different contexts was made with p mimicking the behaviour of the $(p_m)_{m>1}$ sequence, and it was observed its modulus did not converge toward 0 in every cases, and when it did it was with a rate way slower than $1/m$.

It is possible to mimick the behaviour of this error for large values of m by plotting $a \longmapsto |R(a + i\ln(a))|$ (see figures (D.3) and (D.4))

Subsequently, any error made in calculating the p_ms will lead to a strongly divergent additionnal series term proportionate to said error. Since we are bound to have errors in this calculating the p_ms, the non-robustness of the series terms with respect to them will indubitably lead to significative bias on the final solution.

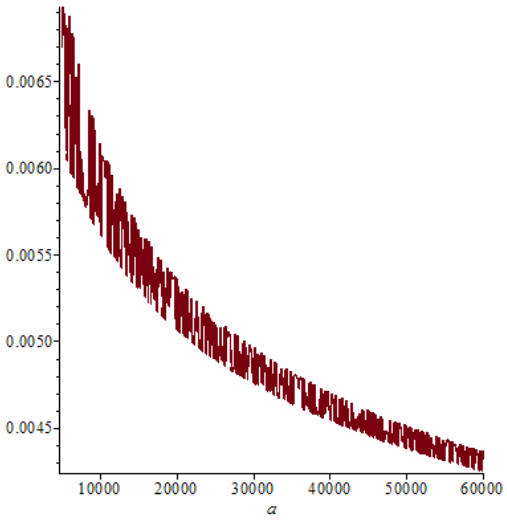

Figure D.1: Plot of the function $a \longmapsto |R(a + i\ln(a))|$

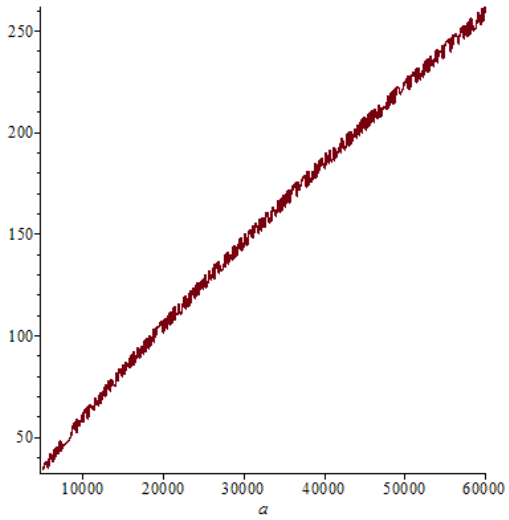

Figure D.2: Plot of the function $a \longmapsto a \times |R(a + i\ln(a))|$

Bibliography

[1] A.Tsuda, R.A. Rogers, P.E. Hydon, and J.P. Butler. Chaotic mixing deep in the lung. *Proc. Nat. Acad. Sci*, 19:10173–10178, 2002.

[2] Shawn C.François L.Shadden and Jerrold.E Marsden. Alternating flow in a moving corner. *Physica D*, 212:272–275, 2005.

[3] K.Moffatt. Viscours eddies near a sharp corner. *Archiwum Mechaniki Stosowanej*, 2, 1964.

[4] K.Moffatt. Local similarity solutions limitations. *J.Fluid.Mech*, 96(2):299–313, 1980.

[5] M.Branicki and K.Moffatt. Evolving eddy structures in oscillatory stokes flow in domains with sharp corners. *Journal of Fluid Mechanics*, 551:63–92, 2006.

[6] J-P.Ovarlez J.Bertrand, P.Bertrand. The mellin transform. http://www.researchgate.net/publication/262875726_The_Mellin_Transform.

[7] F.E.Laine-Pearson and P.E.Hydon. Definition and properties of lagrangian coherent structures from finite-time lyapunov exponents in two dimensional aperiodic flows. *European journal of Mechanics B/Fluids*, 29:278–284, 2010.

[8] M.Branicki and S.Wiggins. Finite-time lagrangian transport analysis : stable and unstable manifolds of hyperbolic trajectories and finite-time lyapunov exponents. *Nonlinear Process in Geophysics*, 17(1):1–36, 2010.